ISSN 1726-5479

SENSORS & TRANSDUCERS

vol. 253
6/21

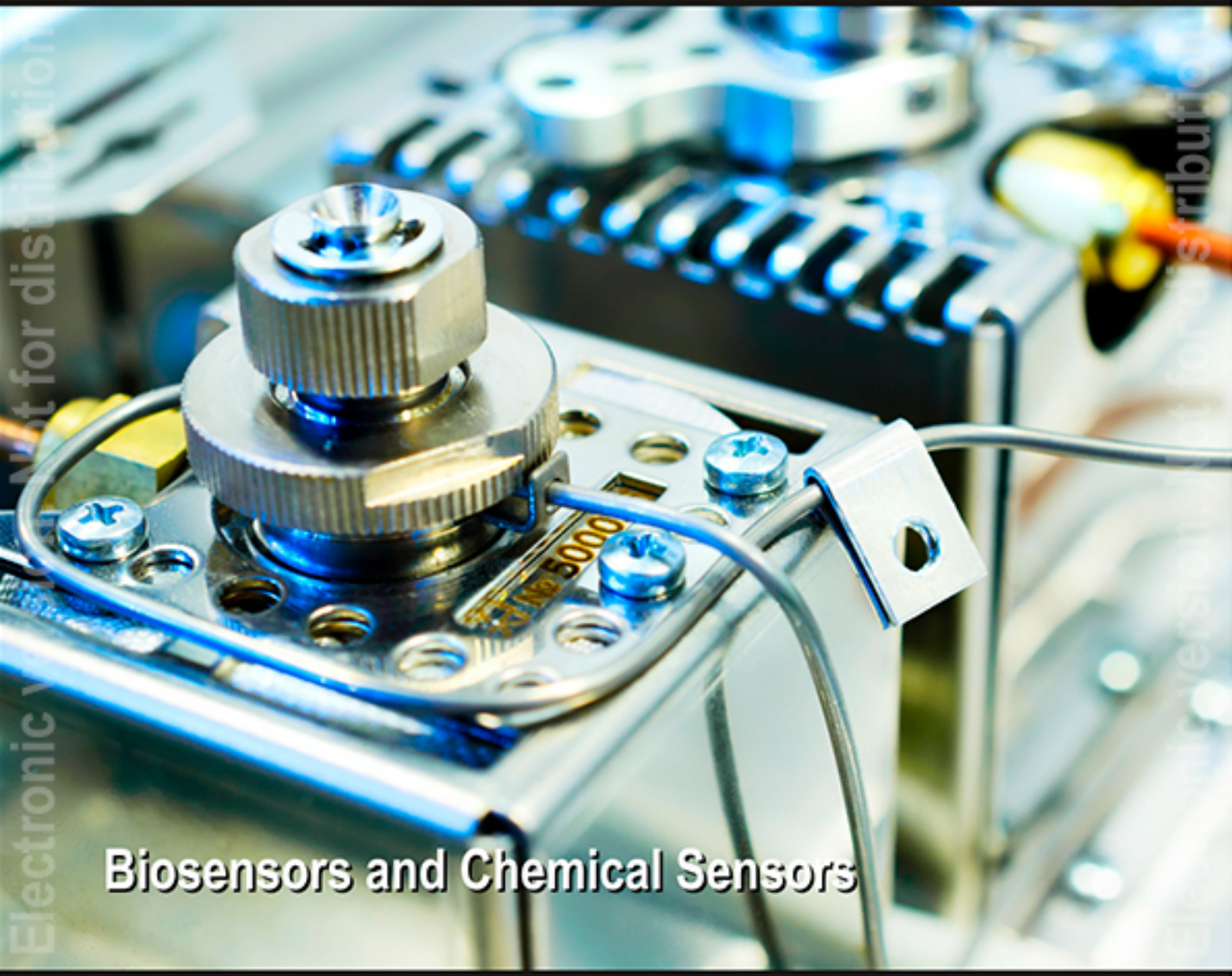

Biosensors and Chemical Sensors

International Frequency Sensor Association Publishing

IFSA

Sensors & Transducers

International Official Open Access Journal of the International Frequency Sensor Association (IFSA) Devoted to Research and Development of Sensors and Transducers

Volume 253, Issue 6, November 2021

IFSA Publishing: Barcelona • Toronto

Published by International Frequency Sensor Association (IFSA) Publishing. Printed in the USA.

Sensors & Transducers

Volume 253, Issue 6
November 2021

www.sensorsportal.com

e-ISSN 1726-5479
ISSN 2306-8515

Sensors & Transducers journal is an open access, peer review international journal published monthly by International Frequency Sensor Association (IFSA).
Available in both: print and electronic (printable pdf) formats.

Sensors & Transducers Journal

Contents

Volume 253
Issue 6
November 2021

www.sensorsportal.com

ISSN 2306-8515
e-ISSN 1726-5479

Research Articles

Short Message

Authors are encouraged to submit article in MS Word (doc) and Acrobat (pdf) formats
by e-mail: editor@sensorsportal.com. Please visit journal's webpage with preparation instructions:
http://www.sensorsportal.com/HTML/DIGEST/Submition.htm

International Frequency Sensor Association (IFSA).

Sensors & Transducers, Vol. 253, Issue 6, November 2021, pp. 1-8

www.sensorsportal.com

Sensors & Transducers

Published by IFSA Publishing, S. L., 2021
http://www.sensorsportal.com

Basic Research on Blood Coagulation Measurement of Extracorporeal Circulation Circuit Using Photoacoustic Imaging of LED Light Source

[1, *] Takahiro Wabe, [2, 3] Ryo Suzuki, [4] Akimitsu Fujii, [5] Yohsuke Uchida, [2, 3] Kazuo Maruyama and [1] Yasutaka Uchida

[1] Teikyo University of Science, Department of Life & Health Sciences, Faculty of Life & Environmental Sciences, 2-2-1 Senjyusakuragi, Adachi-ku, Tokyo, Japan
[2] Faculty of Pharma-Science, Teikyo University, Tokyo, Japan
[3] Advanced Comprehensive Research Organization (ACRO), Teikyo University, Tokyo, Japan
[4] Tokyo College of Medico-Pharmaco Technology, Tokyo, Japan
[5] Shuto iko, Tokyo, Japan
[1] Tel.: 8169101010, fax: + 8169103800
[*] E-mail: takahiro091@gmail.com

Received: 25 October 2021 /Accepted: 27 November 2021 /Published: 30 November 2021

Abstract: In extracorporeal circulation devices such as ECMO, blood coagulation occurs due to various factors. Blood coagulation in the extracorporeal circulation circuit is detected ex post facto by existing pressure sensors. Subsequent detection of blood clots leads to the destruction of blood in the circuit, which is detrimental to the patient. Therefore, for the purpose of preliminary measurement in the extracorporeal circulation circuit, we will conduct basic research on measurement using photoacoustic imaging using LEDs as a light source and report it (AcousticX). As a result of measuring the blood in the extracorporeal circulation circuit circulated using the extracorporeal circulation device by photoacoustic imaging over time, it was found that the wave number and intensity of the photoacoustic wave increased with the passage of time. It has been shown that it is possible to measure the temporal change of blood coagulation circulating in the circuit.

Keywords: Blood coagulation, Photoacoustic imaging, LED, Circuit in an extracorporeal device, Temporal observation, Predictive maintenance.

1. Introduction

ECMO (Extracorporeal membrane oxygenation) is said to be the last bastion for the treatment of severely infected COVID-19 infections. When COVID-19 becomes severe, it is difficult to breathe on its own, and an oxygen mask is insufficient. A ventilator inserts a resin tube through the mouth or throat to deliver oxygen to the lungs and help breathe. In other words, it assists the function of the lungs. After that, when it becomes more serious, the ECMO is connected to the patient. It can also deal with respiratory failure and circulatory failure. The ECMO removes blood from the body, supplies oxygen, excretes carbon dioxide, and returns it to the body. It is a treatment that replaces respiratory and circulatory functions until the patient heals and recovers. In other words, it replaces the function of the lungs, so it is not a radical cure. The configuration of ECMO is shown in Fig. 1.

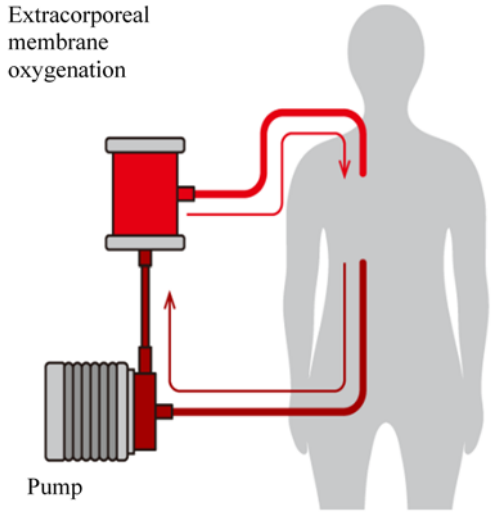

Fig. 1. The configuration of ECMO.

Respiratory failure is the most common cause of death for COVID-19, but the following can also be the cause of death. Causes of death are coagulation activation with excessive immune / inflammatory reactions, so-called cytokine storms, thrombosis, disseminated intravascular coagulation (DIC), and progression to multiple organ failure. [1-5]. In particular, thrombosis and DIC can lead to a rapid deterioration of the condition. Of course, even within the extracorporeal circulation circuit of ECMO, if blood coagulation progresses, it will become clogged and ECMO will not function. Extracorporeal circulation therapy such as ECMO is used in various fields such as heart-lung machines and acute blood purification devices. In the circuit that circulates blood outside the body, blood coagulation occurs due to various factors as described above [6-8]. Various attempts have been made to prevent blood coagulation, and preventive measures using anticoagulants (such as heparin) are currently the mainstream [9-12]. Heparin coatings are used in extracorporeal circulation circuits to suppress coagulation caused by the reaction of blood with foreign bodies [13, 14]. However, since heparin also acts as a foreign substance, it is difficult to completely prevent blood coagulation on the circuit surface. When the circuit is clogged, it is detected by a pressure sensor inside the extracorporeal circuit. However, the detection will be ex post facto because it will be detected after the blood flow in the circuit becomes extremely slow or the circuit is clogged. Subsequent detection of blood coagulation leads to forcing medical staff to take immediate action such as discarding blood in the circuit or replacing the circuit, which is disadvantageous for patients and hospital staff. However, in order to observe changes in blood coagulation status in the extracorporeal circulation circuit in advance, a method with higher sensitivity than the conventional method is required. Therefore, a photoacoustic method was tried as a new measurement method. For the specifications and usage of the photoacoustic method, we referred to the reports of our predecessors. [15-17]. Basic research reports using photoacoustic imaging using LEDs as a light source were conducted at SEIA' 2019 and SEIA' 2020 [18, 19]. In photoacoustic imaging, the measurement target undergoes volume expansion due to the heat generated by the light source, and elastic waves are generated. Elastic waves are received and imaged by ultrasonic probes. The aim of this study is to observe the time course of blood coagulation that occurs in the extracorporeal circulation circuit during blood purification therapy. Since this experiment is a basic experiment, an inexpensive dialysis circuit was used as a circuit measurement target without using an expensive extracorporeal circulation circuit represented by ECMO. Since the dialysis circuit is the same closed circuit as the ECMO circuit, it is considered that there is no difference in measurement. The measurement targets were an air trap to prevent air embolism and a drip chamber equipped with a mesh filter to prevent the generated blood clots from flowing into the body from the extracorporeal circulation circuit. Fig. 2 shows how the blood flow is almost stationary. A drip chamber with slow blood flow is the most suitable measurement target in the circuit because blood coagulates most easily.

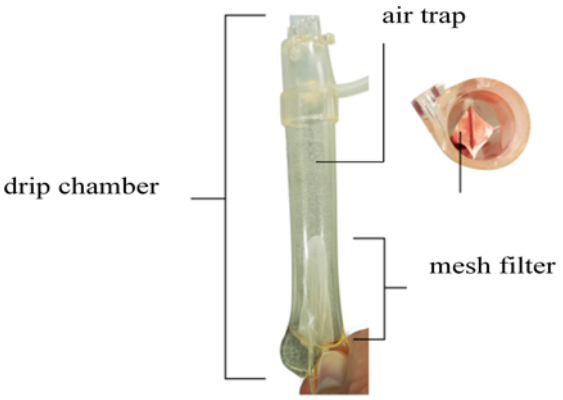

Fig. 2. Drip chamber (overview and cross section).

In a previous research report, blood in a microtube simulating an extracorporeal circulation circuit was measured by photoacoustic imaging with an LED light source. In this paper, we used an extracorporeal circulation device to more practically advance the basic research conducted with microtubes. Using an extracorporeal circulation device, sheep's blood was circulated in the extracorporeal circulation circuit, and the drip chamber was measured by photoacoustic imaging using an LED as a light source.

2. Method

2.1. A-mode Measurement of Solidification Process by Photoacoustic Wave using LED as a Light Source

Fig. 3 shows a schematic diagram of the experimental equipment used in this study. We

examined the measurement of the blood coagulation process in A mode using AcousticX (CYBERDYNE, INC.). Approximately 80 mL of blood was injected into the circulation circuit used in acute extracorporeal circulation therapy. Blood is pumped out by a roller pump and circulates in the circuit. Blood circulates in the circuit at a flow rate of 60 ml/min. The blood temperature was set to 37 °C, which is commonly used in blood purification therapy. The ultrasonic probe used for photoacoustic imaging measurements and the two LED arrays are fixed at about 40 degrees using a jig. The ultrasonic probe and LED were held by hand in the drip chamber to be measured. Regarding the installation of measuring instruments, we refer to the research so far. [18, 20]. The light energy was about 200 μJ/pulse, and the wavelength was 850 nm. There were two types of ultrasonic probes, 10 MHz and 7 MHz. At 10 MHz, the distance resolution improved to some extent, but at 7 MHz, the depth sensitivity increased 4 to 5 times. Therefore, we chose an ultrasonic probe frequency of 7 MHz.

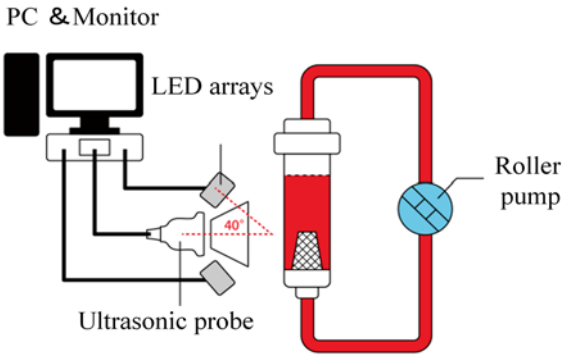

Fig. 3. Configuration diagram of this experiment.

When considering the possibility of a predictive maintenance system, it costs money to use a large amount of blood, and it also takes labor and budget to dispose of it after the experiment. Since a large amount of blood cannot be used at the initial research stage on a budget, I wanted to reduce the amount of blood used as much as possible and increase the number of measurements so that the reproduction of blood coagulation would not be affected. Therefore, in this experiment, the blood used was changed to commercially available sheep blood. Details of the sheep blood used are as follows. Shown in Table 1.

The commercially available blood used is anticoagulant-treated with the anticoagulant ALSEVER'S SOLUTION for transportation. In order to promote blood coagulation, calcium required for blood coagulation is required. By the way, coagulation factors and phospholipids are already contained in blood, so there is no need to add them to commercially available sheep blood. Therefore, we used calcium gluconate as a coagulation accelerator. The upper limit solubility of calcium gluconate is 3.3 g per 100 ml. Infuse 50 ml of blood with 1.1 g of calcium gluconate dissolved in 33 ml of saline.

Table 1. Details of the sheep blood used.

Blood	Aseptic storage blood of sheep
Capacity	100 ml / container
Model number	12070210 Kojin Bio Co., Ltd.
Anticoagulant	Contains anticoagulant (Arsever solution)

2.2. Judgment Criteria When Coagulation Occurs in the Extracorporeal Circulation Circuit

Next, the criteria for determining the occurrence of blood coagulation in the extracorporeal circulation circuit will be described. Since it is difficult to measure the degree of blood coagulation in the circuit during extracorporeal circulation in real time, we observed the following three points where signs of blood coagulation appear in the extracorporeal circulation circuit. These three points are the points used in the medical field to empirically judge the coagulation in the circuit:

1) The blood liquid level in the air trap chamber drops;

2) The venous pressure measured by the pressure sensor decreases;

3) Small bubbles are generated around the roller pump.

2.3. Multidimensional Analysis Based on Photoacoustic Waveform Measurement Modes

Based on the measurement result of A mode measured in 2.1 above, an image is created and the change over time is analyzed. The waveform of A mode measured in the drip chamber is synthesized, and the image of the elastic wave in the entire drip chamber (B mode) is shown. We also converted the B-mode image into 3D and analyzed the photoacoustic waves that occur over time. ImageJ, a free software, was used for both imaging and analysis.

3. Result

3.1. A Mode Measurement

The photoacoustic wave generated from the drip chamber was measured with an ultrasonic probe, and the result of A mode measurement at the point where the intensity of the photoacoustic phenomenon is shown by the red dashed line in Fig. 3 is shown in Fig. 4. The vertical axis represents the intensity of elastic waves generated from photoacoustic phenomena, and the horizontal axis represents the distance from the ultrasonic probe. The part showing the maximum amplitude of the graph is the wall

surface of the drip chamber, the left side is the ultrasonic probe, and the right side is the inside of the drip chamber (blood). In order to measure the time course of the blood coagulation process, immediately after injecting the coagulant into the drip chamber (Fig. 4 (a)), 2 minutes (b), 5 minutes (c), and 10 minutes later (d), the photoacoustic phenomenon of blood was measured separately.

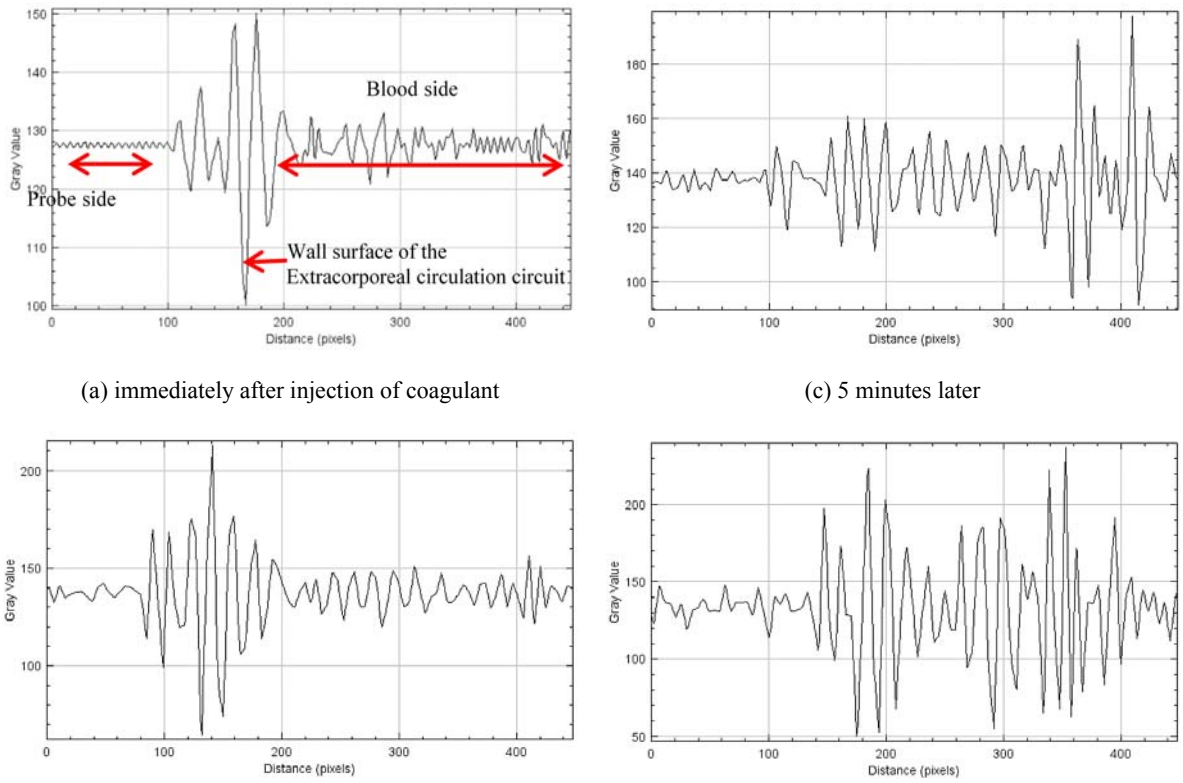

(a) immediately after injection of coagulant

(c) 5 minutes later

(b) 2 minutes later

(d) 10 minutes later

Fig. 4. Measurement of photoacoustic phenomenon using A mode ultrasonic imaging.

3.2. Judgment Criteria When Coagulation Occurs in the Extracorporeal Circulation Circuit

The experimental results are as follows. A slight change was observed about 7 minutes after injecting 1.1 g of calcium gluconate and 33 ml of physiological saline. After 10 minutes, there was a clear change (confirmed the developmental criteria shown in (4)), and after 15 minutes, there was complete blood flow loss. Fig. 5 shows the state around the roller pump after 15 minutes. From the photograph in Fig. 5, the entire circuit becomes negative pressure and is slightly dented. In addition, bubbles can be confirmed in the circuit. Based on these facts, in this study, 10 minutes after injection of calcium gluconate and physiological saline, which is considered to cause the extracorporeal circulation therapy to stop functioning, was set as the time required for blood coagulation in the extracorporeal circulation therapy. The situation at 3 points 10 minutes after injection of calcium gluconate and saline is as follows:

1) Drop of 1.8 cm from the liquid level at the start of the blood level in drip chamber;

2) Negative pressure state (-1 to -10 mmHg) at the start of the experiment: about 60 mmHg;

3) Generation of bubbles (Many bubbles are generated in the red arrow part).

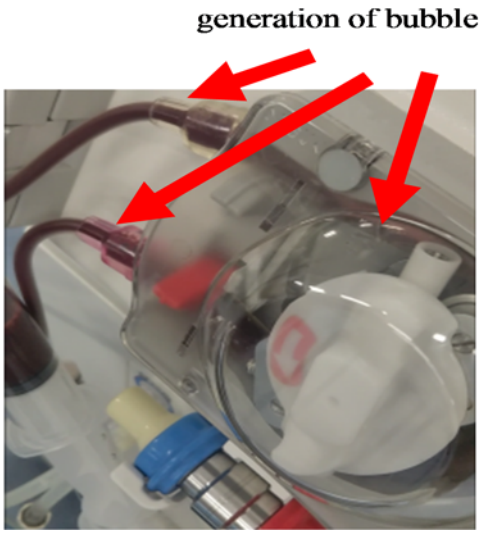

Fig. 5. Bubbles on the pump pull-in side when severe blood coagulation occurs.

3.3. B-mode Measurement and 3D Analysis

3.3.1. B mode

In the drip chamber shown in Fig. 6, the left side of the wall surface is the ultrasonic probe side, and the right side is the blood. The white color (The white color parts) in Fig. 6 indicates that blood obtains light energy and a strong elastic wave is generated by a photoacoustic phenomenon. On the contrary, black (low brightness) indicates that the photoacoustic phenomenon has not occurred or is extremely low. In addition, Fig. 7 shows the measurement results (B mode) reported at SEIA 2019 in order to compare with the time course of blood coagulation in a microtube without blood flow.

3.3.2. 3D Imaging

In order to show the change of blood coagulation over time in Fig. 6 more prominently, the gray scale image in Fig. 6 was converted into a 3D color scale graph as shown in Fig. 8 using the free software ImageJ. Fig. 8 shows the black dotted line points to the wall of the drip chamber.

The right side of the drip chamber wall surface is the blood side (inside the drip chamber), and the left side of the wall surface is the ultrasonic probe side. The x-axis represents the horizontal distance (1 cm from the ultrasonic probe to the blood side), the y-axis represents the vertical distance, and the z-axis represents the pixel brightness (256 levels). The brightness is expressed in 256 steps from 0 to 255. In addition, the low brightness becomes purple, and as the brightness becomes high, it becomes white through orange and yellow. It is considered that the higher the value of the z-axis, the stronger the photoacoustic phenomenon.

4. Consideration

With the passage of time, the position and amplitude of the vibration wave measured by the ultrasonic probe changed. It is considered that the possibility of time-dependent changes due to blood coagulation was shown in the extracorporeal circulation circuit. Comparing to Fig. 6 and Fig. 7, it can be seen that the thick black line is not shown like the microtube wall surface of the B mode image (measurement target: microtube) shown in SEIA2019, and there are ripples. From Fig. 6, the width of the ripples is about 0.2 to 0.3 cm, which is the same as the thickness of the wall surface of the air trap chamber, and from the measurement position, it is considered that the ripples with this width are the wall surface of the air trap chamber. Compared to the micro tube, the wall of the tube is soft and then impedance was almost same as that of the ultrasonic probe gel spacer.

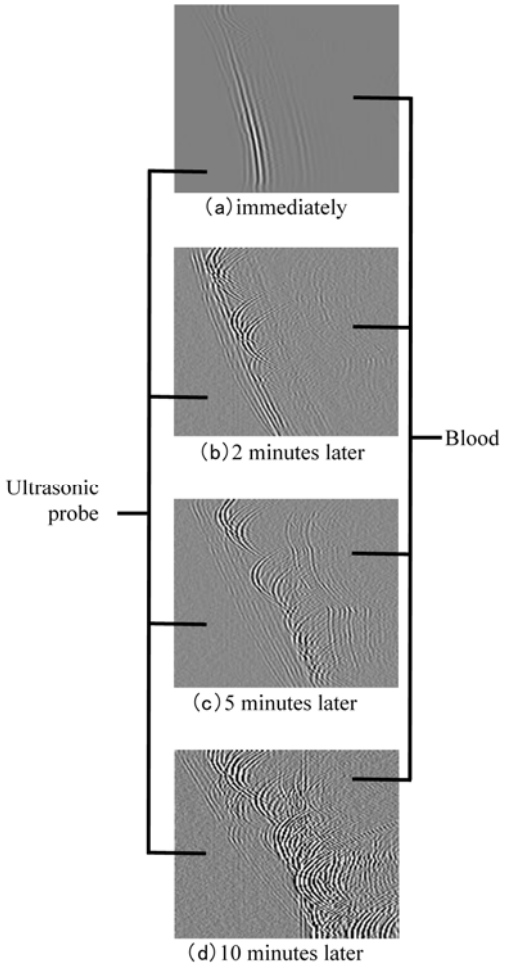

Fig. 6. B mode image by photoacoustic.

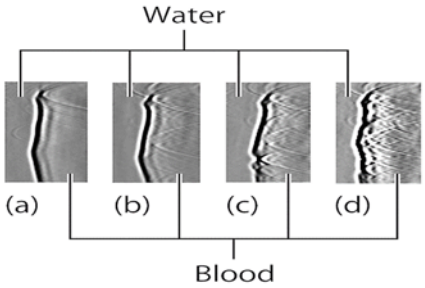

(a) Immediately; (b) 2 minutes later; (c) 5 minutes later; (d) 10 minutes later

Fig. 7. Photoacoustic imaging measurement results reported at SEIA' 2019 (blood coagulation in microtubes).

So it is considered that it was not observed as a thick black line due to wall. Also, the entire B-mode image is slanted. This is because the ultrasonic probe and LED light source do not use a jig and are held and measured by hand. When force was applied to improve the adhesion between the transparent gel spacer and the air trap chamber, the gel spacer was deformed because the transparent gel spacer was soft. From these, it was concluded that the positional relationship between the ultrasonic probe and the object to be

measured was slanted (Fig. 9). Similar results were obtained even if the measurement was repeated while changing the measurer. From the results of this experiment we found that it is important to devise jigs and other devices to apply uniform force.

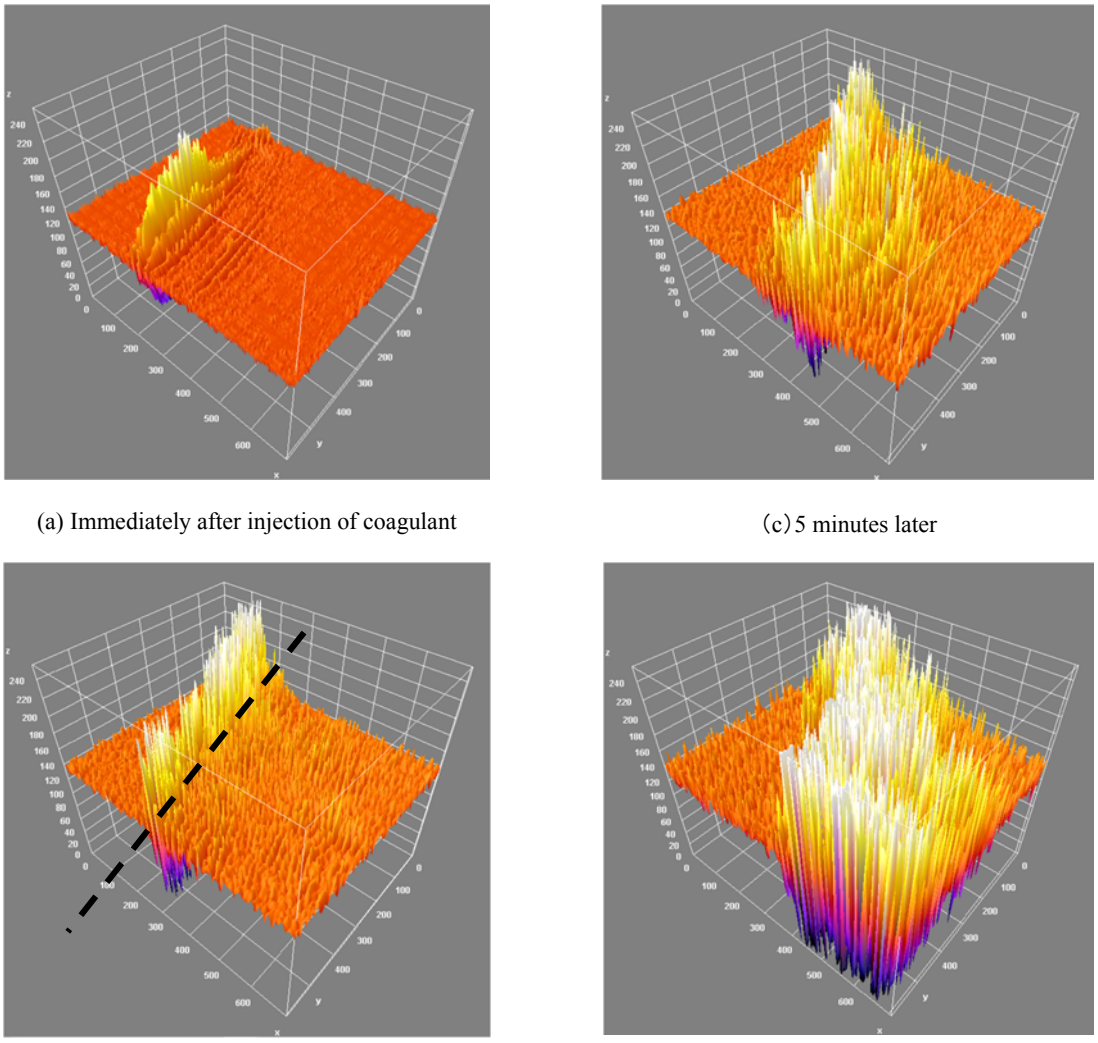

(a) Immediately after injection of coagulant

(c) 5 minutes later

(b) 2 minutes later

(d) 10 minutes later

Fig. 8. 3D diagram of luminance part by ImageJ.

Fig. 9. Measurement diagram of drip chamber.

From Fig. 8 (a) to (d), it can be seen that the brightness (photoacoustic wave) is high centering on the wall surface of the drip chamber. From Fig. 8, it is considered that the increase in blood coagulation could be confirmed from the inner wall where blood reacted with foreign matter and the mesh filter because the parts where the photoacoustic wave changes strongly are on the wall surface and around the mesh filter.

The anticoagulant Alsever was injected into the blood in the drip chamber and the progress was compared. Fig. 10 (a) shows the results of this experiment, Fig. 8 (d), and Fig. 10 (b) shows photoacoustic imaging 10 minutes after injecting Alsever. It was found that even in the presence of blood flow, no photoacoustic wave is generated when the blood is not coagulated.

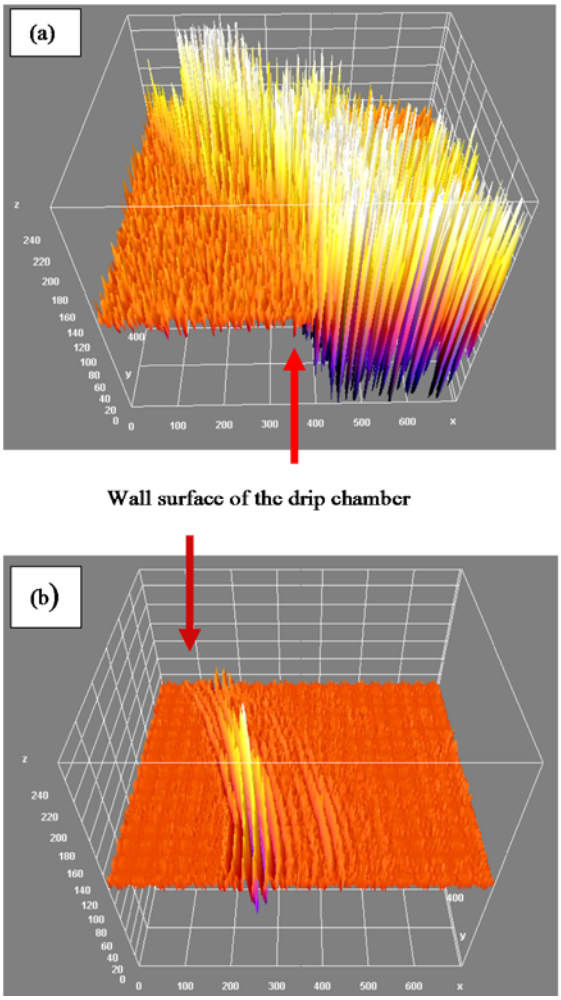

Fig. 10. Comparison of blood coagulation in the drip chamber and blood containing anticoagulant: (a) 10 minutes after blood coagulation begins, (b) 10 minutes after injecting the anticoagulant.

5. Conclusions

We measured the blood coagulation as the changes of the whole extracorporeal circulation circuit, using photoacoustic imaging, instead of measuring individual blood clots. As with the measurement results of changes in blood coagulation in microtubes in SEIA 2019 over time, changes in blood coagulation in the extracorporeal circulation circuit can be measured using the extracorporeal circulation circuit, and demonstrated the possibility of predictive maintenance in extracorporeal circulation therapy. In addition by using LED photoacoustic imaging. We showed the possibility of simple measure machine with a small sensor.

Acknowledgments

T. Wabe and Y. Uchida would like to thank Mr. N. Sato of CYBERDYNE, INC Research and Development Dept, for his cooperation in this experiment.

References

[1]. N. Tang, Dengju Li, X. Wang, Z. Sun, Abnormal coagulation parameters are associated with poor prognosis in patients with novel coronavirus pneumonia, *J. Thromb. Haemost.*, Vol. 18, 2020, pp. 844-847.

[2]. P. Mehta, D. F. McAuley, M. Brown, E. Sanchez, R. S. Tattersall, J. J. Manson, HLH Across Speciality Collaboration, UK: COVID-19: Consider cytokine storm syndromes and immunosuppression, *Lancet*, Vol. 395, 2020, pp. 1033-1034.

[3]. Ricardo J. Jose, Ari Manuel, COVID-19 cytokine storm: The interplay between inflammation and coagulation, *Lancet Respi. Med.*, Vol. 8, Issue 6, 2020, pp. e46–e47.

[4]. D. J. M. Wright, Prevention of the cytokine storm in COVID-19, *Lancet Infect Dis*, Vol. 21, Issue 1, 2020, pp. 25-26.

[5]. T. Iba, J. H. Levy, M. Levi, J. M. Connors, J. Thachil, Coagulopathy of coronavirus disease 2019, *Crit. Care Med.*, Vol. 48, Issue 9, 2020, pp. 1358-1364.

[6]. J. Utley, Pathophysiology of cardiopulmonary bypass: Current issues, *Cardiac Surgery*, Vol. 5, Issue 3, 1990, pp. 177-189.

[7]. Y. Mori, Blood compatible material, *Kobunshi Ronbunshu*, Vol. 4, No. 42, pp. 601-615, October 1985 (in Japanese).

[8]. J. K. Kirklin, A. D. Pacifico, Complement and the damaging effects of cardiopulmonary bypass, *J. Thorac. Cardiovasc. Surg.*, Vol. 86, Issue 6, 1983, pp. 845-857.

[9]. L. Gott, J. D. Whiffen, R. C. Dutton, Heparin bonding on colloidal graphite surfaces, *Science*, Vol. 142, Issue 3597, 1963, pp. 1297-1298.

[10]. I. O. Salyer, Medical Application of Plastic, in Biomedical Material Symposium, No. 1, *Interscience,* New York, Vol. 105, 1971.

[11]. M. Murase, A. Usui, M. Maeda, Y. Tomita, F. Murakami, K. Teranishi, T. Koyama, T. Ito, T. Abe, Nafamostat mesilate reduces blood loss during open heart surgery, *Circulation*, Vol. 88 (5 Pt. 2), pp. 11432-11436, November 1993.

[12]. M. Hiroura, A. Usui, M. Kawamura, M. Hibi, K. Yoshida, F. Murakami, J. Iwase, Nafamostat mesilate reduces bloodcell adhesion to cardiopulmonary bypass circuit: an in-vitro study, *J. Extra Corpo.r Technol.*, Vol. 26, Issue 3, 1994 September, pp. 121-125.

[13]. L. K. von Segesser, B. M. Weiss, El. Garcia, A. von Felten, M. I. Turina, Reduction and elimination of systemic heparinization during cardiopulmonary bypass, *J. Thorac. Cardiovasc. Surg.*, Vol. 103, Issue 4, 1992, pp. 790-798.

[14]. V. Videm, T. E. Molines, P. Garred, J. L. Svennevig, Biocompatibility of extracorporeal circulation. In vitro comparison of heparin-coated and uncoated oxygenator circuits, *J. Thorac. Cardiovasc. Surg.*, Vol. 101, Issue 4, 1991, pp. 654-660.

[15]. H. Zhong, T. Duan, H. Lan, M. Zhou, F. Gao, Review of low-cost photoacoustic sensing and imaging based on laser diode and light-emitting diode, *Sensors*, Vol. 18, Issue 7, 2018, p. 2264.

[16]. T. J. Allen, P. C. Beard, High power visible light emitting diodes as pulsed excitation sources for biomedical photoacoustics, *Biomedical Optics Express*, Vol. 7, Issue 4, 2016, pp. 1260-1270.

[17]. A. B. Karpiouk, S. R. Aglyamov, S. Mallidi, J. Shah, W. G. Scott, J. M. Rubin, S. Y. Emelianov, Combined ultrasound and photoacoustic imaging to detect and stage deep vein thrombosis. phantom and ex vivo studies, *J. Biomed. Opt.*, Vol. 13, Issue 5, September-October 2008, 054061.

[18]. T. Wabe, R. Suzuki, K. Maruyama, Y. Uchida, Possibility for temporal observation of thrombus generated in extracorporeal circulator circuit by photoacoustic imaging using LED, in *Proceedings of the 5th International Conference on Sensors Engineering and Electronics Instrumentation Advances (SEIA'19)*, Canary Islands (Tenerife), Spain, 25-27 September 2019, pp. 157-160.

[19]. T. Wabe, R. Suzuki, K. Maruyama, Y. Uchida, The Measurement of Blood Coagulation Process in Extracorporeal Circuit Using LED Photoacoustic Imaging, *Sensors & Transducers*, Vol. 237, Issue 9-10, September-October 2019, pp. 88-94.

[20]. T. Wabe, R. Suzuki, K. Maruyama, Y. Uchida, Possibility of Extracting Feature Value from the Changes in Brightness over Time of Blood Coagulation in the Extracorporeal Circuit, *Sensors & Transducers*, Vol. 246, Issue 7, November 2020, pp. 64-70.

Sensors & Transducers, Vol. 253, Issue 6, November 2021, pp. 9-17

www.sensorsportal.com

Sensors & Transducers

Published by IFSA Publishing, S. L., 2021
http://www.sensorsportal.com

Gas Sensor Based on Biohydroxyapatite to Study the Volatile Compounds of Nasal Secretion

[1, *] Tatiana KUCHMENKO, [1, 2] Ruslan UMARKHANOV, [1] Anastasiia SHUBA and [3] Dariya MENZHULINA

[1] Voronezh State University of Engineering Technologies,
19 Revolution Avenue, 394039 Voronezh, Russia
[2] LLC "Sensorika – Novye Technologii", 19 Revolution Avenue, apt. 1, 394039 Voronezh, Russia
[3] Voronezh Children's Clinical Hospital named after N. N. Burdenko
16 lane Health, Voronezh, Russia
Tel.: +7(473)255-42-67, fax: +7(473)255-42-67
E-mail: tak1907@mail.ru

Received: 25 October 2021 /Accepted: 25 November 2021 /Published: 30 November 2021

Abstract: The paper investigates the properties of gas sensors based on biohydroxyapatite for diagnostic the state of the upper respiratory tract of calves and humans. The process of synthesis of biohydroxyapatite of different mass is described. The peculiarities of sorption of volatile compounds on this sorbent depending on mass are considered for two modes of measurement (injection and frontal). The effectiveness and selectiveness of organic vapor microweighting using biohydroxyapatite phases of different mass are estimated. Possibilities of volatile organic compounds vapors identification in a mixture without separation are considered. For this task, the new parameters are calculated by the signals of one or two piezoelectric sensors with biohydroxyapatite of different masses. Results of analysis and identification of substances in the gas phase over nasal secretions of calves and humans with various respiratory diseases are presented. The intervals of the values of the calculated parameters are determined for reliable selection of samples into the "inflammation" group. The first and second order errors have been estimated in binary classification into groups "healthy" and "inflammation". The minimum number of false-positive responses in the classification of samples is achieved using the parameters of two sensors with a biohydroxyapatite of different masses.

Keywords: Sensors, Biohydroxyapatite, Sorption, Volatile organic compounds, Diagnostics, Upper respiratory tract, Inflammation, Nasal secretion.

1. Introduction

When analyzing biological samples, it is essential to minimize the number of analysis stages and the changes in the native state of the samples by preparation for measurement (heating, sorption, extraction, freezing). The use of an array of sensitive gas sensors ("electronic nose" or E-nose) simplifies preparation stages as much as possible and allows to fix the integral profile of the most informative part of the metabolome - volatile compounds. This approach has been widely used to analyze various human and animal samples over the past ten years [1].

The most popular biosamples for analysis are exhaled air, blood, urine, sweat, saliva and others [2-5]. Also, it was established that the nasal secretion of calves is an informative biosample as the exhaled breath condensate when diagnostic of respiratory

diseases by detecting volatile compounds using arrays of piezoelectric sensors [6-8]. The results are relevant and valuable for developing portable devices for on-farm diagnosis [9].

We believe that the approach is universal and can be extended to human biosamples. It is vital for monitoring the inflammation of the lungs and larynx in humans when infected with viruses, including SARS-CoV-2 and E-nose technologies are perspectives for that [10].

Using the new materials for sensitive coatings of measurement elements in E-nose increases the stability, sensitivity, operating time and expands the possibilities of sensors application in various conditions [11-12].

Earlier, the parameters of sorption of volatile compounds using the phase of biohydroxyapatite were implemented to analyze the results of sorption of the gas phase of nasal secretion samples [13].

This work aims to investigate the features of sorption of volatile compounds by biohydroxyapatite phases of different masses and apply the sensors based on it to estimate the presence of upper respiratory tract inflammation by analysis of gas phases over human and animal nasal secretions.

2. Materials and Objects

The study was carried out on the device "MCNanoW-PQ" (LLC "Sensorika – New Technologies", Voronezh, Russia) with eight working channels [14]. The multichannel device is connected with a laptop via the MCW-Soft for registering changes in the biohydroxyapatite phase mass in real-time with a step of 1 s and a sensitivity of 1 ng. Multichannel nanobalances are equipped with a sealed fluoroplastic cell with a volume of 60.0 cm^3 with a cap and nozzles for introducing vapors, both individual compounds and their mixtures in different modes – frontal, injection. Piezoelectric quartz resonators (PQR) with a base frequency of 10.0 and 14.0 MHz were used to manufacture sensors.

The phase of hydroxyapatite (HA) was studied as a sorbent. Hydroxyapatite $Ca_5(PO_4)_3OH$ was obtained by the sol-gel technique developed at the University named after N. I. Lobachevsky [15]. Reagent concentrations were optimized to obtain nanoparticles with good sorption properties [16].

The hydroxyapatite phase from acetone (0.5 g of phase/10 ml) was uniformly deposited to the electrodes of the piezoelectric quartz resonator, defatted with acetone, by immersion in an ultrasonic suspension [17]. The mass of the phases from 1 to 7 μg was obtained by varying the exposure time of the resonator in the suspension (from 5 to 15 s) to control the sensitivity and selectivity of microweighing of substances vapors. The free solvent was removed in an oven (40 minutes at t from 50 °C), placing the PQR in the holder vertically. Hydroxyapatite synthesized by the sol-gel method is a nanostructured material compatible with biological tissues; therefore, we assumed its unique sorption properties to volatile biomolecules that are excreted during the life of organisms. The microstructure of HA coatings was investigated on a Solver P447-PRO (CJSC "NT-MDT", Russia) atomic force microscope (AFM) with a video surveillance system to substantiate and explain the dependence of the sorption properties of HA of different mass.

Vapors of individual volatile organic compounds were selected as sorbats (LLC "Reakhim", Russia): (VOCs): aliphatic alcohols C_2–C_5, normal and isomeric structure; ketones (acetone, methyl ethyl ketone), arenas (benzene, toluene, phenol), amines (methylamine, diethylamine), aliphatic acids C_2, C_4, C_5; chloroform, C_2-C_5 alkyl acetates, acetaldehyde. We also investigated the sorption of water vapor (bidistillate, with electrical conductivity control) as the main component of biosample, which can interfere with the detection of analytes.

The vibration frequency of the quartz plate changes during sorption of substances on the HA phases, deposited on the PQR electrodes. According to the Sauerbrey model, the change in the vibration frequency of the piezoelectric sensor ($-\Delta F_{max}$, Hz) is proportional to the mass of the sorbate Δm (μg) on its electrodes at any moment of sorption time. This model was also used to calculate the mass of the sorbent phases on the piezoelectric balance electrodes (m_{HA}, μg) as mentioned in [16].

The mass of individual volatile compounds during sorption is measured at a temperature of (20.0 ± 0.5 °C) using two modes of vapor input (Fig. 1). In the injection mode, a 5.0 cm^3 sample of an individual substance was placed in a glass sealed vessel, which was closed with a soft polymer membrane and kept for 20-30 min at a temperature of (20 ± 1) ºC until equilibrium was established in the "liquid – vapor" system. After that, a certain volume of the equilibrium gas phase (EGP) over the substance was taken by an individual syringe and introduced into the detection cell of the device at a rate of 1 cm^3/s. The mass concentration of vapors of substances in the detection cell was varied by changing the volume of the EGP from 0.5 to 5.0 cm^3 with a step of 0.5 cm^3.

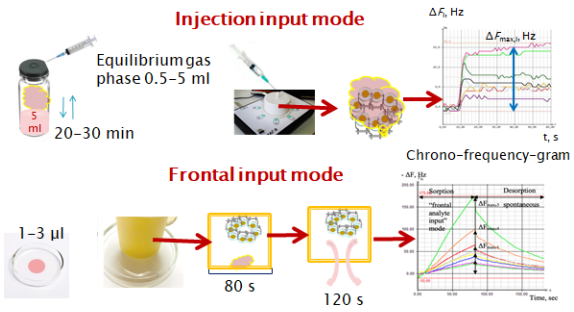

Fig. 1. The scheme of sorbtion measurement.

The VOC vapor sorption for each concentration was measured 5-7 times. After checking the system's stability and starting the measurement, the vapors

were introduced into the near-sensor space. The frontal mode of vapor input into the detection cell was carried out under static conditions (without a carrier gas) due to spontaneous diffusion of vapors into the near-sensor space from the source (sample of an individual compound) in a closed nozzle body. The particular volume of substances (from 1 to 3 μl for each substance) was placed onto the glass Petri plate and covered by the detection cell of the device with sensors for 80 seconds. Substances were evaporated entirely during that time, the response of sensors were recorded in the 80 s. After that, the detection cell was opened for the spontaneous desorption of gases from sensor coverings. The mass concentrations, frontal input mode of measurement are more completely described in work [8].

To calculate the sorption parameters $A(i/j)$ [18], we used a quantitative signal of piezoelectric balances with a sorbent — the maximum change in the oscillation frequency of the piezoelectric sensor ($-\Delta F_{max}$, Hz), which characterizes the efficiency of sorption of compounds on the sorbent phases.

Samples of nasal secretion from calves (n=50) and humans (n=17) were selected using sterile cotton swabs. Samples of calf's nasal secretion were simultaneously investigated by bacteriological and molecular-genetic methods. The animals were auscultated and clinically examined by specialists according to Wisconsin respiratory scoring chart [19]. The study was conducted according to the guidelines of the Declaration of Helsinki, and approved by the Ethic Committee of Voronezh State University of Engineering Technologies (protocol № 2 dated 25 February 2021). The clinical examination of the volunteers by the specialist established the presence or absence of inflammation in humans.

The group of "inflammation" consisted of samples from animals with bovine respiratory disease (n=10) (diagnosis based on results of clinical and laboratory examination) and from a human with the first sign of respiratory disease according to anamnesis and clinical examination (n=10). The "healthy" group included samples from animals (n=40) and humans (n=7) without any signs of respiratory disease.

The nasal secretion samples were measured by frontal input mode under static conditions due to spontaneous diffusion of vapors into the near-sensory space of the detection cell from biosamples.

3. Results and Discussion

3.1. Microstructural Investigation of Hydroxyapatite Phases

The microstructure of HA coatings of different mass was investigated by atomic force microscopy with a video surveillance system to understand the features of the sorption properties (Fig. 2). Based on the images obtained in the Nova 1.0.26.143 program (freely available), the average grain diameter and roughness were calculated (Table 1).

Table 1. Microstructural characteristics of HA coatings.

Mass of coating, μg	Average diameter of grain, nm	Roughness, nm
2.03	415	544
4.17	215	111
5.03	187	97

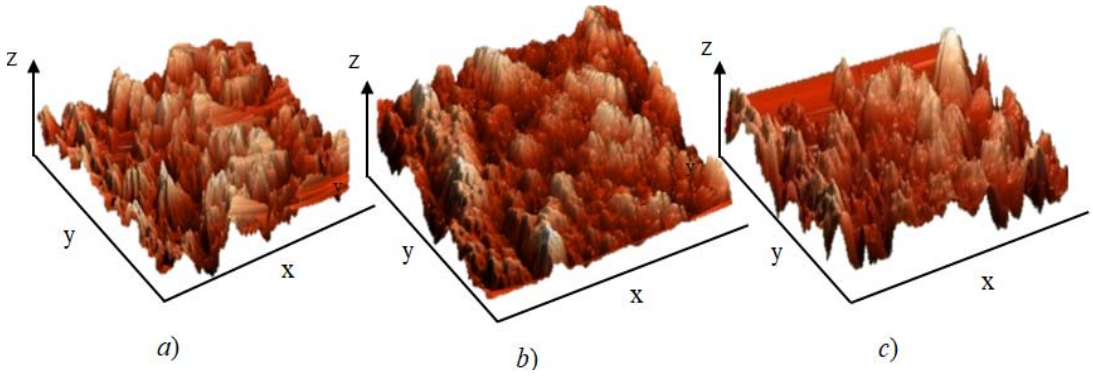

Fig. 2. Image of HA phases obtained in Nova program using AFM with resolution: 30×30 μm. Mass of HA m=2.19 μg (a); 4.17 μg (b); m=5.03 μg (c).

It was found that for HA with an increase in the coating mass, the average grain diameter and roughness decrease. It turns out that for coatings of HA with a different mass, a surface of different porosity is formed, which determines the variation in sorption properties of the coatings. It was also found that an increase in the mass of the HA coating by more than 4 μg does not lead to significant changes in the average grain size on the surface and roughness. This makes it possible to predict reproducibility and similar sorption properties with insignificant changes in coating weights of more than 4 μg, which is important for the industrial production of sensors with reproducible, repeatable properties.

3.2. Sorption Properties of the Hydroxyapatite Phase of Different Masses

Earlier it was established on the example of solid-state sorbents of different nature [14, 20-21] that an increase in the mass of phases on the electrodes of piezoelectric resonators has a different effect on the sensitivity of microweighing of water vapors and organic compounds. The dependence of the rate of change in the maximum sensor response on the mass of the hydroxyapatite phase on the electrodes was studied using several biomolecules of different polarity and injection input mode (Fig. 3).

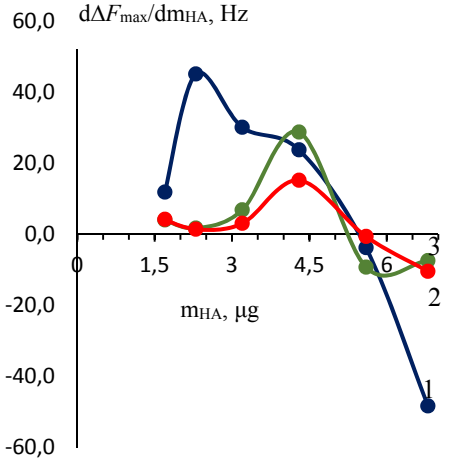

Fig. 3. Dependence of the rate of change of the maximum response of sensors on the mass of HA on the electrodes in vapors: water (1), ethanol (2), acetone (3).

The rate of change in the analytical signal per unit mass of the HA phase is proportional to the rate of sorption of analytes for a fixed time of loading the system. The rate of change in the analytical signal of the sensor in the vapors of all three compounds depends on the mass of HA, but in different ways for water and organic biomolecules (ethanol, acetone). Phases of small masses (1-2 μg) and big (more than 5 μg) react equally ineffectively to vapors of all compounds. The highest rate of change in the signal of a sensor with 2.0-3.5 μg mass HA is characteristic of water vapor, while the sensor reacts slowly to organic compounds in this mass range. The rate of change in the analytical signal of the sensor for all compounds is equal for sensors with a 3.5-5.5 μg HA phase.

Nevertheless, varying the coating mass is more critical for weighing water vapor than for ethanol and acetone. This fact is helpful in microweighing the vapors of biomolecules of organic compounds against the background of water. Furthermore, using two sensors with a small and big mass of the HA phase makes it possible to separately indicate ethanol and acetone vapors in a sample with any concentration of water vapors. This approach allows us to speak of separate microweighing of biomolecules without separation by at least two sensors with HA phases.

Further, to study the sorption properties of HA coatings, sorption isotherms were constructed and studied (Fig. 4). The isotherm shape for HA phases of different masses changes from linear to S-shaped for the same sorption system. In this regard, it is impossible to describe the curves by a single theory: linear isotherms were described according to Langmuir's theory and S-shaped by polymolecular adsorption theory (BET-theory) (Table 2).

Based on the obtained results, an increase in adsorption (a) is observed in the homologous series of alcohols C_2H_5OH-$C_5H_{11}OH$ during sorption on the HA. At the same time, the number of adsorbed centers per unit mass of the adsorbent increases, and due to this, the sorption process proceeds much better. Using calculated monolayer capacity, it can be concluded that the HA phase exhibits the best sorption properties to water, propanol-1, butanol-1.

It is challenging to analyze the peculiarities of the mechanism of interaction of even homologues on the same sorbent phase using the obtained isotherm. The differences in the character of isotherms for one sorbent with different characteristics of the surface make it possible to estimate changes in the filling of pores of different nonideal phase geometry. Henry coefficient K_a, Hz*dm^3/mol is a priority characteristic of the systems under consideration since it characterizes the sensitivity of piezoelectric sensors to a particular type of vapor (Table 2). It was found that the values of the K_a coefficient for water vapor, butanol-1 depend on the mass of the sorbent phase, while for other compounds, within the limits of the microweighing sensitivity error, they are indistinguishable or change insignificantly. The affinity for butanol-1 molecules changes especially sharply in the HA phases of small (1-2 μg) and large masses (4-5 μg). If we take into account that the roughness of the surface of the HA phase also changes sharply (Table 1), it can be argued that for a linear alcohol molecule the surface parameters are defining the sorption character.

The sensitivity of microweighing increases with an increase in the number of carbon atoms in the alkyl radical of alcohol. A decrease in the polarity of alcohol molecules with an increase in the length of the alkyl radical reduces the effect of hydrogen bonds during sorption, but at the same time, it is on the rougher surface of low-mass phases that heavy alcohols are more efficiently sorbed. The obtained correlation for alcohols is stable and is consistent with the theoretical foundations of piezoelectric quartz microweighing. The nature of the change in the sensitivity of piezoelectric balances with low mass HA allows predicting an increase in sensitivity with further growth of the alkyl radical in the alcohol molecule.

For a sorbent phase of small masses (2-3 μg), the sensitivity of microweighing of vapors of substances decreases in the following sequence: alcohols> acetone> water> diethylamine> benzene.

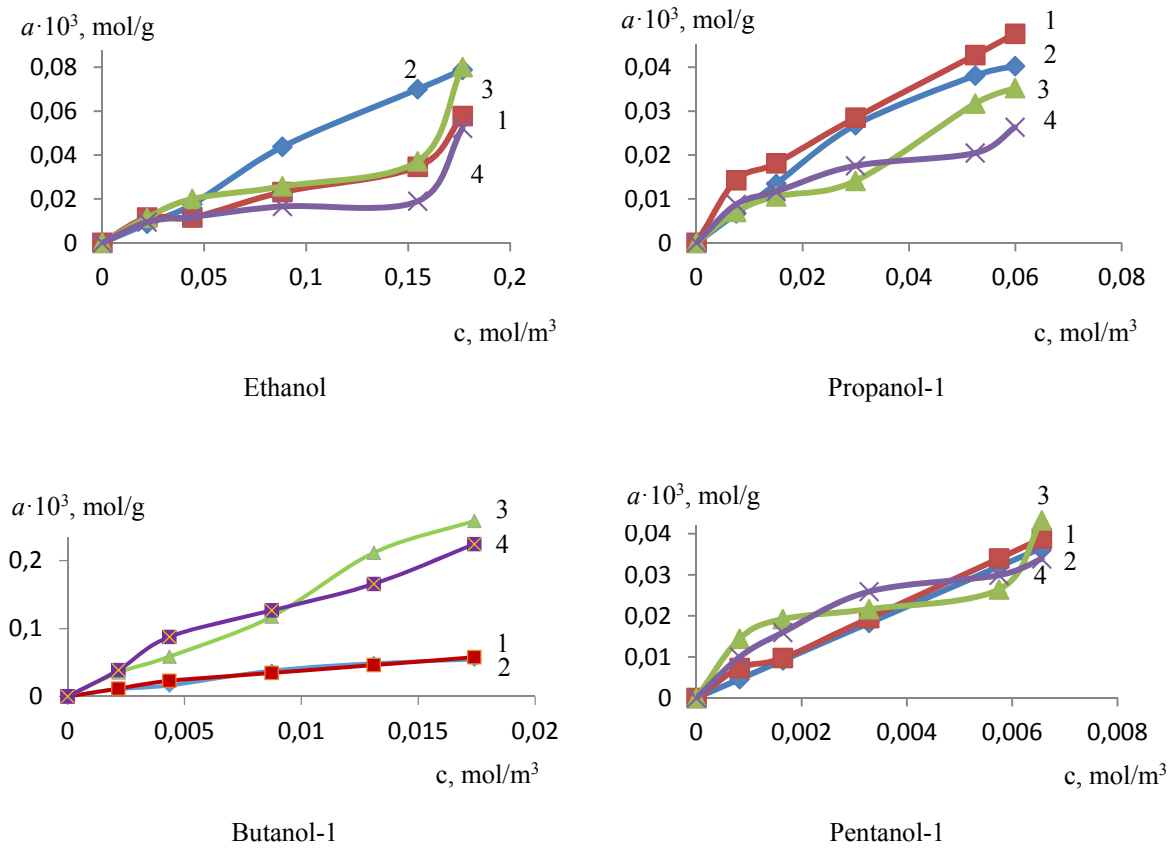

Fig. 4. Isotherms of alcohols vapor sorption on the HA phases of different mass: 1 – m=1.03 μg; 2 – m=2.19 μg, 3 – m=4.17 μg; 4 – m=5.03 μg.

Table 2. Constants of sorption isotherm of volatile compounds on the HA coatings with different mass.

Sorbtives	Lengmuir's model		BET theory	
	Mass of coating, m_{HA}, μg	Henry coefficient K_a, Hz·dm³/mol	Mass of coating, m_{HA}, μg	Constant C_{BET}, dm³/mol
Water	1.03 2.15	6.4 2.0	4.17 5.03	32 16
Ethanol	2.15	4.5	1.03 4.17 5.03	5.4 8.9 20
Butanol-1	1.03 2.15 4.03 5.03	36 35 15 13	-	-
Butanol-2	1.03 2.15	12 10	4.17 5.03	38 57
Pentanol-1	1.03 2.15	59 56	4.17 5.03	98 34
Acetone	1.03 2.15	0.7 0.8	4.17 5.03	2.1 1.4
Diethylamine	2.15 4.03 5.03	0.4 0.4 0.2	1.03	1.1

For sorbent phases of big masses (4-5 μg), the efficiency of microweighing decreases in the following order: phenol >> alcohols C_4-C_5 > water > chloroform > ethanol, acetone > benzene > diethylamine.

The mass sensitivity sequences for the small and big mass phases of biohydroxyapatite are not identical. This confirms the participation in sorption not only of the chemical sorption centers but also of pores, channels, and rough surfaces of HA phases to a greater

extent than for carboxylated carbon nanotubes and polymer sorbents [22-23].

The method of vapor input (injection or frontal) also significantly affects selectivity. It was found that with the injection of vapors of the studied compounds, the HA phase with a mass of 4-5 μg is most selective to vapors of ethanol, acetone, amines, amyl acetate, and acids, and the phase with a mass of 2-3 μg is most selective to vapors of methylamine, benzylamine, and acetic acid. In the frontal mode of vapor input, selectivity was noted for many biomolecules upon sorption on the small mass HA phase than on the big mass HA phase.

The possibility of identifying the studied vapors of substances with simultaneous microweighing with piezoelectric balances with different masses of the HA phase has been demonstrated in Table 3. The parameters of the sorption efficiency A(i/j) [8, 18] were calculated for sensors with the HA phase of different masses – A_m(i/j), where i, j are the mass of the phase (μg). In Table 1, the values of the parameters of the sorption efficiency are highlighted in bold, which can be used to solve problems of identification of individual substances in a mixture and correspond to requirements for identification parameters [8-9]. Thus, the identification parameters for water and phenol is the parameter A_m(i/j) for sensors with HA phase of small masses (1 and 3 μg). The simultaneous use of a small (1 μg) and a big mass (4-5 μg) of the HA phase makes it possible to identify propanol-1 and benzene in the mixture (Table 3).

Table 3. Parameters of the sorption efficiency of vapors (A_m(i/j)) of substances on piezoelectric balances with a HA phase of different masses in the injection mode.

Analytes	Values of HA mass in μg for parameter A_m(i/j)				
	1/2	1/4	1/5	2/4	4/5
Water	**3.2**	0.20	0.40	**0.06**	1.6
Ethanol	1.2	0.61	0.27	0.51	0.45
Propanol-1	1.1	0.86	**0.14**	0.80	**0.16**
Propanol-2	2.0	0.52	0.91	0.26	1.8
Butanol-1	1.0	0.24	0.28	0.23	1.2
Butanol-2	1.2	0.32	0.21	0.26	0.67
Pentanol-1	1.1	-	-	-	0.67
Benzene	0.95	**1.1**	2.1	1.1	2.0
Phenol	**0.69**	0.79	1.7	1.1	2.2

The mode of vapor injection into the detection cell significantly changes the identification parameters of biomolecules. A_m(4/2) identification parameters were calculated for 2 μg and 4 μg masses of the HA phase at the injection and frontal input mode (Table 4).

The overlap of the identification parameter values using the coincidence criterion [9, 18] at different modes of vapor input was established for water, acetone, benzene, methylamine, ethylacetate, and acetic acid (Table 4). The differences are significant for other compounds, and the identification parameters obtained under different sorption conditions cannot be applied. It is explained the different character of dependence of the sensor signal on the concentration of the analyte in the detection cell and near sensory space. Vapors of acetone, benzene, methylamine, ethyl acetate, acetic acid have a linear dependence of the sensor signal on the concentration of the substance in the studied range. For vapors with nonlinear dependence of the sensor signal on the concentration of the substance (alcohols, phenol, chloroform, diethylamine), the differences in the values of the parameters are significant.

Table 4. Parameters A_m(4/2) with injection and frontal mode of vapors input into detection cell, F_0 = 10.0 MHz.

Analytes	Injection input mode	Frontal input mode	Coincidence criterion
Water	1.0	1.1	0.3
Ethanol	0.25	0.52	0.08
Propanol-1	0.40	0.70	0.12
Propanol-2	0.38	1.3	0.26
Butanol-2	0.33	0.65	0.12
Pentanol-1	0.29	0.90	0.16
Acetone	0.25	0.17	0.09
Methylethylketone	1.00	0.55	0.14
Benzene	0.45	0.31	0.15
Phenol	0.25	0.74	0.14
Chloroform	0.43	1.5	0.28
Methylamine	2.5	1.7	0.9
Diethylamine	0.08	0.54	0.12
Ethylacetate	0.88	1.1	0.24
Acetic acid	1.2	1.5	0.6
Butyric acid	0.40	0.18	0.12

The results correspond to the theoretical and practical foundations of sorption interactions. Therefore, an approach for identifying individual analytes in a mixture by comparing the identification parameters of standard test substances and calculated for analyzed samples obtained under identical experimental conditions is acceptable.

The frontal mode of vapors input allows identifying more substances in the mixture than the injection input. For the analysis of biosamples, comparison of their state, and assessment of changes in time, the most promising is the frontal input mode of highly volatile compounds, which significantly simplifies the experiment and practically eliminates sample preparation.

3.3. Nasal Secretion Analysis

Clinical examination and analysis of biological samples by laboratory methods made it possible to classify animals by the degree of damage to the respiratory organs [7, 9]. The array included sensors with phases of biohydroxyapatite of different masses (4.0 μg and 2.0 μg). According to the measurement results, the values of the parameter A_m(4/2) were

calculated for 50 samples of nasal secretions of calves and the informative values of this parameter for ranking into groups "healthy", "inflammation" from the respiratory organs were found out (Table 5) with an assessment of classification errors for the systems with a binary response [24]. The numerical values of the calculated parameter $A_m(4/2)$ for sensors with HA phases help to identify individual test substances in samples and divide them into groups (Tables 4, 5). It was found that only for one range of values of this parameter, the proportion of false-positive assignments of samples from the "healthy" group to the "inflammation" group is equal to zero. For nasal secretion samples of the "inflammation" group, volatile compounds were identified (amines, alcohols, ketones, arenas). These compounds are markers of inflammation and protein destruction [8].

The versatility of the approach to assessing the state of the upper respiratory tract using highly volatile compounds of human nasal secretion was tested on 17 samples. In this case, the ranking of the samples into the "inflammation" group was carried out according to the range of the parameter $A_m(4/2) = 0.60 – 0.67$ (Table 6).

Table 5. Parameter $A_m(4/2)$ with the frontal mode of vapors input from nasal secretion samples of calves, $F_0 = 10$ MHz.

Calf stock number and diagnostic group	**Range of parameter $A_m(4/2)$ values**	**Identified compounds**	**Proportion of correct positive (false negative) answers**	**Proportion of correct negative (false positive) answers**
"Healthy": 2663, 2661, 2655, 2432, 2657, 2650, 2438, 2671, 2670, 2669, 2666 "Inflammation": 2646	0.77 – 0.9	No compounds dominating in concentration	- (0.1)	0.28
"Healthy": 2428, 2659, 2658, 2661, 2675 2443, 2437, 2659, 2667, 2662, 2647, 2668, 2657, 2664, 2653, 2442, 2662, 2676, 2677, 2674, 2679, 2675, 2674, 2673 "Inflammation": 2439, 2665, 2469	1.0 – 1.4	Propanol-2	- (0.3)	0.6
"Healthy": 2652, 2430, 2653, 2652, 2679 "Inflammation": 2672	1.5 – 1.8	Methylamine, acetic acid	- (0.1)	0.12
"Healthy": - "Inflammation": 2666, 2660, 2665, 2669, 2663	**0.60-0.67**	Diethylamine, ethanol, propanol-1, butanol-2, phenol, methylethylketone	0.5	- (0)

Table 6. Classification of human nasal secretion samples by parameter $A_m(i/j)$ for two sensors with 2 and 4 μg of HA.

Sample number	**Value of parameter $A_m(4/2)$**	**Assignment to the "inflammation" group according to the values of the parameter $A_m(4/2)$**	**Condition based on clinical examination**
1	0.63	Yes	Inflammation
2	0.63	Yes	Healthy
3	0.59	Yes	Inflammation
4	0.20	No	Healthy
5	0.63	Yes	Inflammation
6	0.67	Yes	Inflammation
7	1.0	No	Dry nose, secretion is almost absent
8	0.71	Yes	Healthy
9	0.83	No	Healthy
10	0.63	Yes	Inflammation
11	0.63	Yes	Inflammation
12	0.67	Yes	Inflammation
13	0.63	Yes	Inflammation
14	0.67	Yes	Inflammation
15	0.63	Yes	Inflammation
16	0.91	No	Healthy
17	0.77	No	Healthy
-	0.77	-	Water
-	1.0	-	Container

The proportion of correct ranking of human secretions samples in the "inflammation" group according to the selected numerical boundaries of the parameter $A_m(4/2)$ is 0.91. The proportion of false attribution for the considered sample is 0.25 due to the small size of the sample. However, the high sensitivity of assigning samples to the "inflammation" group confirms the correctness and versatility of the approach. The first and second order errors have been estimated in binary classification based on sorption parameters for sensors with HA. The sensitivity and specificity of classification were 100 and 86 %, respectively.

4. Conclusions

The study of the sorption of organic compounds and water vapors by phases of hydroxyappatite of different masses on the piezoelectric resonators is allowed to formulate a new approach to changing the selectivity of microweighing of VOCs.

A new identification principle in "electronic nose" system is proposed using one effective sorbent of different masses to identify VOCs in a mixture without separation.

The frontal mode of vapors input creates conditions similar to gas chromatography to recognize components in a mixture with a much simpler and faster instrumental solution.

The proposed sorption parameters could be applied to rapidly assess the inflammation presence in the upper respiratory tract of animals and humans. The correctness of the interpretation of the results was confirmed by the clinical examination and laboratory analysis results. The success of applying the approach in the analysis of biological samples of animals and humans opens up new prospects for out-of-laboratory diagnostics.

Acknowledgments

The research was supported by Russian Science Foundation, grant number 18-76-10015.

References

[1]. A. D. Wilson, Noninvasive Early Disease Diagnosis by Electronic-Nose and Related VOC-Detection Devices, *Biosensors,* Vol. 10, Issue 7, 2020, 73.

[2]. M. Fleischer, E. Simon, E. Rumpel, H. Ulmer, V. Harbeck, M. Wandel, C. Fietzek, U. Weimar, H. Meixner, Detection of volatile compounds correlated to human diseases through breath analysis with chemical sensors, *Sensors and Actuators B: Chemical,* Vol. 83, Issue 1-3, 2002, pp. 245-249.

[3]. M. Milanowski, P. Pomastowski, T. Ligor, B. Buszewski, Saliva - Volatile Biomarkers and Profiles, *Critical Reviews in Analytical Chemistry,* Vol. 47, Issue 3, 2017, pp. 251-266.

[4]. M. Monteiro, N. Moreira, J. Pinto, A. S. Pires-Luis, R. Henrique, C. Jeronimo, M. D. Bastos, A. M. Gil, M. Carvalho, P. G. de Pinho, GC-MS metabolomics-based approach for the identification of a potential VOC-biomarker panel in the urine of renal cell carcinoma patients, *Journal of Cellular and Molecular Medicine,* Vol. 21, Issue 9, 2017, pp. 2092-2105.

[5]. R. Xue, L. Dong, S. Zhang, C. Deng, T. Liu, J. Wang, X. Shen, Investigation of volatile biomarkers in liver cancer blood using solid-phase microextraction and gas chromatography/mass spectrometry, *Rapid Communications in Mass Spectrometry,* Vol. 22, Issue 8, 2008, pp. 1181-1186.

[6]. T. A. Kuchmenko, A. A. Shuba, R. U. Umarkhanov, E. V. Drozdova, A. E. Chernitskii, Application of a piezoelectric nose to assessing the respiratory system in calves by volatile compounds, *Journal of Analytical Chemistry*, Vol. 75, Issue 5, 2020, pp. 645-652.

[7]. T. A. Kuchmenko, A. A. Shuba, R. U. Umarhanov, A. E. Chernickij, "Electronic nose" signals correlation evaluation for nasal mucus and exhaled breath condensate of calves with the clinical and laboratory indicators, *Analitika I Kontrol' [Analytics and Control]*, Vol. 23, Issue 4, 2019, pp. 557-562.

[8]. T. Kuchmenko, A. Shuba, R. Umarkhanov, L. Lvova, The New Approach to a Pattern Recognition of Volatile Compounds: The Inflammation Markers in Nasal Mucus Swabs from Calves Using the Gas Sensor Array, *Chemosensors*, Vol. 9, Issue 6, 2021, 116.

[9]. T. Kuchmenko, A. Shuba, R. Umarkhanov, A. Chernitskiy, Portable Electronic Nose for Analyzing the Smell of Nasal Secretions in Calves: Toward Noninvasive Diagnosis of Infectious Bronchopneumonia*, Veterinary Sciences,* Vol. 8, Issue 5, 2021, 74.

[10]. S. Dragonieri, G. Pennazza, P. Carratu, O. Resta, Electronic Nose Technology in Respiratory Diseases, *Lung,* Vol. 195, Issue 2, 2017, pp. 157-165.

[11]. D. Goyal, S. K. Mittal, A. Choudhary, R. K. Dang, Graphene: A two dimensional super material for sensor applications, *Materials Today-Proceedings*, Vol. 43, 2021, pp. 203-208.

[12]. T. Wasilewski, B. Szulczynski, M. Wojciechowski, W. Kamysz, J. Gebicki, Determination of long-chain aldehydes using a novel quartz crystal microbalance sensor based on a biomimetic peptide*, Microchemical Journal*, Vol. 154, 2020.

[13]. T. Kuchmenko, R. Umarkhanov, A. Shuba, D. Menzhulina, The Application of Gas Sensor with Biohydroxyapatite to Study the Volatile Profile of Nasal Secretion, in *Proceedings of the 7th International Conference on Sensors and Electronic Instrumentation Advances (SEIA' 2021),* Mallorca, Spain, 22-24 September 2021, pp. 56-61.

[14]. T. Kuchmenko, R. Umarkhanov, D. Menzhulina, Biohydroxiappatite – new phase for selective micro weighing of organic compounds - inflammation markers. First communication: Sorption in model mixtures, *Sorbtzionnye I Khromatograficheskie Protzessy [Sorption and Chromatographic Processes],* Vol. 21, Issue 2, 2021, pp. 142-152.

[15]. E. N. Bulanov, Obtaining and investigation of nanostructured boicompatible materials based on hydroxyappatite, *Nizhnii Novgorod University*, 2012 (in Russian).

[16]. A. A. Shuba, T. A. Kuchmenko, R. U. Umarkhanov, A. E. Chernitskiy, Portable E-nose for Diagnostic of Inflammation and Diverse Variation in Health Status

of Humans and Animals, in *Proceedings of the 5th International Conference on Advances in Sensors, Actuators, Metering and Sensing (ALLSENSORS 2020)*, Valencia, Spain, 16 - 22 March 2020, pp. 56-62.
[17]. Korenman Ya. I., Silina Yu. E., Kuchmenkko T. A. Method for modifying the electrodes of a piezoquartz resonator, *Patent 2259007 RU*, issued 29.01.2004.
[18]. T. Kuchmenko, A. Shuba, N. Belskich, The identification parameters of organic substances in multisensors piezoquartz microbalance. *Analitika I Kontrol' [Analytics and Control],* Vol. 16, Issue 2, 2012, pp. 151-161.
[19]. S. M. McGuirk, Disease management of dairy calves and heifers, *Veterinary Clinics of North America: Food Animal Practice*, Vol. 24, Issue 1, 2008, pp. 139-153.
[20]. T. A. Kuchmenko, R. U. Umarkhanov, Cornejo Tueros Jose Vladimir, Investigation of sorption properties of carboxilated nanotubes on piezoelectric microbalance BAW-type, *Sorbtzionnye I Khromatograficheskie Protzessy [Sorption and Chromatographic Processes],* Vol. 21, Issue 3, 2021, pp. 336-346.
[21]. T. A. Kuchmenko, Electronic nose based on nanoweights, expectation and reality, *Pure and Applied Chemistry,* Vol. 89, Issue 10, 2017, pp. 1587-1601.
[22]. Shogenov Yu. Kh., T. A. Kuchmenko, S. S. Grazhulene, Features of sorption of alcohols mixtures of normal and isomeric structure on the carbon nanomaterials, *Sorbtzionnye I Khromatograficheskie Protzessy [Sorption and Chromatographic Processes],* Vol. 9, Issue 3, 2009, pp. 416-423.
[23]. T. A. Kuchmenko, R. U. Umarkhanov, Peculiarities of microweighing of trace quantities of alkylamines on polymer and solid-state thin films, *Journal of Analytical Chemistry*, Vol. 68, Issue 4, 2013, pp. 368-375.
[24]. Yu. V. Kholin, N. A. Nikitina, A. V. Panteleimonov, Ye. A. Reshetnyak, A. A. Bugaevskii, L. P. Loginova, Metrological characteristics of binary response detection techniques, *Timchenko Publ.*, 2008.

Sensors & Transducers, Vol. 253, Issue 6, November 2021, pp. 18-22

www.sensorsportal.com

Sensors & Transducers

Published by IFSA Publishing, S. L., 2021
http://www.sensorsportal.com

Development of a Fluorescence-based Biosensor for Coumaphos

Fabiana TORTORA, Elena PORZIO, Carmen GALOPPO, Ferdinando FEBBRAIO and * Giuseppe MANCO
Institute of Biochemistry and Cell Biology, Via P. Castellino 111, 80131, Italy
Tel.: 0816132698, fax: 0816132706
E-mail: giuseppe.manco@cnr.it

Received: 2021 /Accepted: 2021 /Published: 30 November 2021

Abstract: A screening procedure has been implemented based on the inverse virtual screening technique to identify new bioreceptors for the set-up of pesticide biosensors. Different pesticides of interest were docked on a limited database of proteins with known 3D structures. Some compounds of interest were chosen among the following classes: organophosphates, organo-clorurates, carbamates, anilides, neonicotinoids, aromatic and heterocyclic azoto-organics. Hundreds of molecules were automatically docked on hundreds of structures and results analysed. We identified many interesting binders among which we focused on an *E. coli* helicase that was demonstrated to be able to bind the organophosphate Coumaphos on multiple sites. In addition we report on the purification of the binder and testing with Coumaphos and other compounds in a fluorescence-based assay.

Keywords: Helicase, Pesticides, Docking analysis, Bioreceptor, Biosensor, Fluorescence-based assay.

1. Introduction

Frequently, in the last decades, the community has been facing the problems arising from the transfer of potentially harmful substances to the environment, altering the ecosystem, and to the human, causing pathological symptoms, and sometimes, death [1]. Recently, the European Union has banned the use of some compounds thought to be carcinogenic [2]. Nevertheless, some of these compounds, as pesticides, are necessary and useful to the human well-being. Pesticides represent an example of toxic molecules intentionally released into the environment with the aim of preventing, destroying and removing pests.

Their diffusion is not limited only to the agricultural sector, but also to houses and public areas of cities, representing a great risk to the environment and human health [3].

Pesticides can be classified on the basis of their function (insecticides, fungicides, acaricides, herbicides, plant growth regulators) and/or their chemical structure in: Organophosphates (OP), Organochlorines (OC), Carbamates (CMs), Neonicotinoids, Anilides, Aromatic and Heterocyclic AzoOrganics. In Table 1 the general chemical structures for the main pesticide families are shown.

Some actions have been undertaken; for example, this century has marked the disappearance in the environment of the highly persistent organochlorine pesticides, gradually replaced by organophosphates and carbamates that, in spite of a lower resistance to degradation, have become the most diffuse neurotoxic chemical compounds. The mechanism of action of these neurotoxic compounds concerns mainly the irreversible inhibition of acetylcholinesterase [4], a key enzyme for the correct activity of the nervous

system. Other pesticides have different mechanisms of action. Because of toxicity to humans, the removal of excess of these compounds from the environment is mandatory, but a preliminary action of detection and monitoring is also required. Over the last decades, different biosensors have emerged as ultra-sensitive and rapid techniques for environmental monitoring and food quality control [2, 5]. These tools have the potential to complement or replace the classical analytical methods by simplifying or eliminating sample preparation protocols and making the testing in the field easier and faster with a significant decrease of the analysis costs. Unfortunately, most of the available biosensors are not su□ciently robust to deal with raw samples and do not o□er adequate selectivity. For these reasons we started a project for the identification and testing of new bioreceptors for different classes of pesticides, in particular for the organophosphate Coumaphos [6].

Table 1. Pesticides classification based on chemical structure.

ORGANOPHOSPHATES	
ORGANOCLORINATED	
CARBAMATES	
ANILIDES	
NEONICOTINOIDS	
HETEROCYCLIC AZOTORGANICS	
AROMATIC AZOTORGANICS	

Coumaphos is one of the main pesticides of concern for the health of bees. It is a widely available organophosphate-based acaricide formulated by Bayer into CheckMite strips and Perizin®. Beekeepers introduce these coumaphos products into colonies to control parasitic varroa mites (*Varroa destructor*). Coumaphos acts systemically when small quantities of it are ingested by bees, with consequent trophic diffusion.

However, most of the acaricide is distributed colony-wide within 3 h through dermal contact among nestmates [7].

In fact, acaricides like Coumaphos are non-pathogenic external agents widely used by beekeepers, so Coumaphos residues are often found in products like bee bread, propolis, wax, comb and royal jelly, the latter being a vital foodstuff for brood and queen rearing [8, 9]. The acute lethal dose (LD50) of Coumaphos for individual bees varies from 3 to 6 μg, with lower doses proving more toxic to older bees [7]. Chronic exposure to Coumaphos can result in reduced foraging activity, affect the size of hypopharyngeal glands, and increase the level of programmed cell death within bee tissues [8]. Although Coumaphos is regarded as being weakly toxic to honey bees, more study is needed to determine whether this acaricide decreases individual bee survival and hence the health of the pollinator workforce. Coumaphos is classified as an extremely hazardous substance in the United States and is subject to strict reporting requirements by facilities which produce, store, or use it in significant quantities [10].

2. Identification of Coumaphos as a Binder

2.1. Docking Analysis

A screening procedure has been implemented based on the “inverse virtual screening” technique to identify new bioreceptors for the set-up of pesticide biosensors. In particular, a docking analysis was conducted through the use of scripts in the Linux bash shell, via the command line, which invoked the AutoDock Vina software, with a series of parameters defined in a configuration file. Specifically, the script accessed the workbook relating to a specific family of pesticides, and for each file "ligand_name.pdbqt" associated a "protein_name.pdbqt" file, transferring the files generated with the configuration parameters of the number of models to be created to AutoDock Vina software. For each analysis an output of the possible protein-ligand conformations was generated, with the respective binding energies, and a file containing the corresponding ligand structures in space. The output files were always analyzed with the help of scripts in the Linux bash shell, in order to identify the conformations with the greatest affinity for binding.

A cut-off of -6.0 kcal/mol for the binding energies was established with reference to the minimum free energy values obtained from the in silico measurements of EST2 with the pesticides that experimentally showed greater affinity [11].

Different pesticides of interest were docked on a limited database of proteins with known 3D structures. We have set up automatic procedures for docking and analysis of hundreds of molecules on hundreds of structures (Fig. 1) (manuscript in preparation).

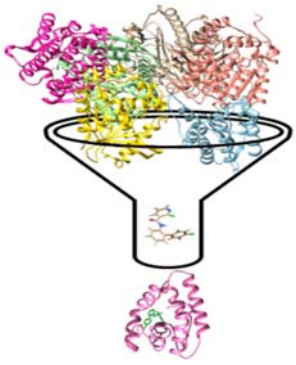

Fig. 1. Computational docking analysis "inverse virtual screening" approach.

Coumaphos emerged as a good binder of the protein Helicase RecQ from *E. coli* with a binding energy of about -6.4 kcal/mol.

From the data analysis, the C-terminal domain of helicase RecQ (HRDC domain) (ID PDB: 1WUD) was demonstrated to bind Coumaphos on three sites (Fig. 2 A, B). The energy interaction (-6.4 kcal/mol; site 1 Fig. 2 C) was the best we detected among all the organophosphate compounds.

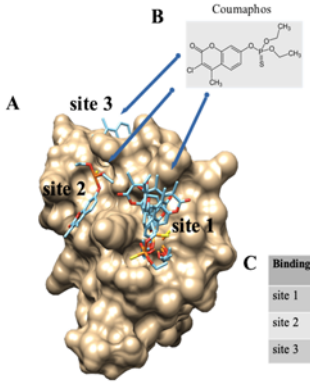

Binding sites	Energy interaction (kcal/mol)
site 1	-6,4
site 2	-6,0
site 3	-5,8

Fig. 2. Results of the docking analysis of the HRDC domain with Coumaphos. (A) Coumaphos binding sites on the HRDC domain. (B) Chemical structure of Coumaphos. (C) Table of the interaction energies in kcal/mol of the three binding sites.

3. Cloning, Expression, and Purification of the HRDC-RecQ Domain in *E.Coli*

The plasmid vector used for the *in vitro* expression of the HRDC-RecQ domain of *E. coli* is the plasmid pET28b (+), which was provided by Prof. James L. Keck from the Department of Biomolecular Chemistry (BMC) of the University Wisconsin School of Medicine and Public Health - Madison, WI - United States. For cloning, *E. coli* (Invitrogen) competent Top10 cells were used, with high replication efficiency, while for gene expression, the recombinant plasmid was hosted by *E. coli* BL21 (DE3) cells.

3.1. Protein Purification

The recombinant protein was purified by affinity chromatography with immobilized metal ions (IMAC, Immobilized Metal Affinity Chromatography) (manuscript in preparation). The highly selective technique is based on the formation of specific bonds between the biological macromolecule of interest and a metal ion (ligand), immobilized on the stationary phase. In the specific case, a nickel resin (Ni-NTA) (Quiagen) was used as the stationary phase, i.e. functionalized with chelating groups loaded with divalent Ni2+ ions, with which the histidines, through their imidazole ring, can establish coordination bonds. The protein was eluted from the column with 200 mM Imidazole, which competes with the protein in binding to the resin.

Purification of the recombinant protein was completed by removing residual impurities by molecular exclusion chromatography. Gel filtration chromatography was conducted using an ÄKTA-FPLC (GE Amersham Pharmacia) system, using a HiLoad ™ 16/600 Superdex ™ 75 PG column (GE Healthcare) with a capacity of 120 mL. The column has a highly cross-linked dextran and agarose matrix. The strong selectivity of dextran and the high chemical and physical stability of the agarose allows high-resolution separations. The chromatography was performed by equilibrating the column in 20 mM Tris-HCl pH 8.0 buffer, the sample was loaded into the same running buffer by applying a flow of 0.5 mL/min, and fractions of 1 ml volume were collected (Fig. 3).

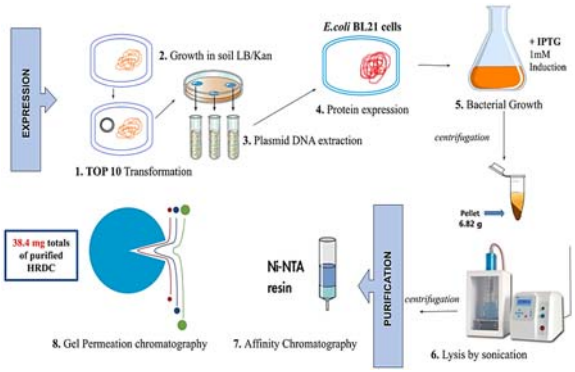

Fig. 3. Expression and Purification of the HRDC domain. 1-4. Transformation of E. Coli TOP10 and BL21 cells for cloning and expression of the HRDC-RecQ domain gene, respectively. 5. Induction of protein expression by Isopropyl-β-D-1-thiogalact-pyranoside (IPTG). 6-8. Cell lysis and purification of the protein domain.

4. HRDC Domain Labeling and Fluorescence Analysis

The domain sequence was modified by site-directed mutagenesis to change the exposed serine 575 into a cysteine for the binding of the IAEDANS fluorescent probe [12]. The main site-directed mutagenesis technique uses the experimental implantation of Polymerase Chain Reaction (PCR). In fact, oligonucleotides are produced, which act as primers, containing the desired mutation. Therefore, we designed the forward and reverse oligonucleotides in the wild-type sequence of the HRDC domain. The mutant is obtained by replacing a serine residue with a cysteine residue at position 575 of the amino acid sequence. The oligos were ordered and supplied by the Eurofin/Genomics Company and used as primers for PCR. Then, I ran various rounds of PCR based on the characteristics of the Wonder Taq HOT Start (Hot Start Thermostable DNA polymerase) enzyme. Subsequently, I performed the enzymatic digestion with the restriction enzyme Dpn1, specific for

methylated DNA, in order to digest the parental DNA. The mutant sequence was controlled for any additional mutations introduced accidentally.

We expressed and purified the two proteins with the procedure described above.

The wild-type protein was quite soluble and stable. In contrast, the mutant had some stability problems because of a tendency of the protein to aggregate. After appropriate dilution below 0.15 mg/ml, the protein domain was proven to be much more stable.

Therefore we proceeded with the optimization of the IAEDANS binding under the following conditions: 1 mg of the protein was dialyzed with buffer 20 mM Tris/HCl pH 8.0 containing 0.5 mM Tri-n-butyl phosphine (TBP) and incubated with IAEDANS under the conditions indicated in Table 2.

Table 2. Optimization of the IAEDANS binding.

Condition No.	Incubation Time	Temperature	Molar Ratio (protein:probe)	AUF/ug
1.	Over night	4 °C	1:50	
2.	Over night	4 °C	1:10	
3.	3h	37 °C	1:10	
In the presence of Imidazole	3h	37 °C	1:10	380
In the absence of Imidazole	3h	37 °C	1:10	95

Condition No. 3 was found to be the best in terms of specific fluorescence intensity and responsiveness to quenching by using a Jasco FP-8200 spectrofluorometer (Jasco, Tokyo, Japan) at room temperature; in particular, the labeling carried out in the presence of Imidazole (6 mM) gave an increase of specific fluorescence intensity (Fig. 4). The labeled protein was stable for at least 30 days at 4 °C and the specific fluorescence activity was around 380 AUF (Arbitrary Unit of Fluorescence)/µg. The graph shows a biphasic trend of fluorescence quenching for Coumaphos in a semilogarithmic plot suggesting the presence of heterogeneous binding sites in agreement with the docking analysis. The biphasic behavior was independent of the Imidazole thus suggesting different interaction sites.

After optimization, we tested the labeled domain by quenching of fluorescence with Coumaphos and Paraoxon as a control.

As reported in Fig. 5, Coumaphos at 300 nM gave a 30 % quenching of fluorescence whereas under the same conditions paraoxon was almost ineffective.

5. Conclusions

Pesticides are among the most common contaminants in the environment. Although their use is necessary to protect crops, their constant presence in the various matrices represents one of the main environmental problems, as they can compromise the health of humans and animals.

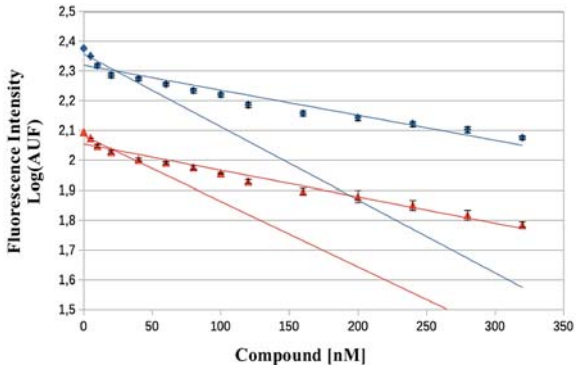

Fig. 4. Quenching of fluorescence by Coumaphos of protein labeled with IAEDANS in the presence (blue line) or in the absence (red line) of Imidazole. The fluorescence signal of the labeled protein significantly improved in presence of Imidazole.

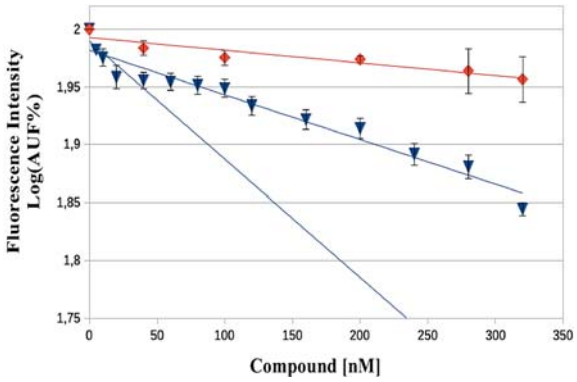

Fig. 5. Quenching of fluorescence intensity by Paraoxon (red point) or by Coumaphos (blue point). The interfering effect of acetonitrile (in which pesticides were dissolved) has been subtracted.

To Protect the environment and public health, each year the European Food Safety Association (EFSA) prepares reports to be able to verify the maximum residue limits (MRLs) on food products, intended for human and animal consumption. Due to the presence of various pesticide residues not approved by the European Union and the persistence of their potentially toxic metabolites in the various environmental matrices, EFSA has motivated research on toxicological studies and the development of new detection systems. An example is Coumaphos, a pesticide to which EFSA turned its attention due to the persistence of its metabolites in water and soil. To optimize risk management throughout the country, however, it is necessary to develop systems that are efficient, fast, cheap, and easy to use, such as biosensors. As a consequence, it is necessary to identify new bioreceptors capable of binding potentially toxic substances, belonging to the various pesticide families, which can then be used for the design of a multi-biosensor system. The study of the *in vitro* interactions of the HRDC domain with toxic molecules supports the results obtained from bioinformatics analyses, opening up new perspectives. Although these studies are still preliminary the data

stimulate further analysis, intending to be able to consider this domain in the future as a possible bioreceptor in a biosensory system.

Our results indicate that the methodology used was good for identifying new bioreceptors to be exploited for the development of specific biosensors. Furthermore, the improvement of the specific fluorescence intensity of the labeled protein in the presence of imidazole suggests a conformational change induced by imidazole, which we will have to evaluate. We are currently testing other pesticides to confirm the specificity of the bioreceptor.

Acknowledgments

This paper was supported by the POR Campania PON03PE_00060_4 "Prodotti Alimentari" and MUR POC01_00042 “SIABIO” grants to G. M.

We thank Prof. James L. Keck and Dr. Brian Ferrer from the Wisconsin University Dept. of Biomolecular Chemistry (USA) for the plasmid (pET28b +) containing the HRDC domain.

References

[1]. F. Febbraio, L. Merone, G. P. Cetrangolo, M. Rossi, R. Nucci, G. Manco, Thermostable Esterase 2 from *Alicyclobacillus acidocaldarius* as Biosensor for the Detection of Organophosphate Pesticides, *Analytical Chemistry*, Vol. 83, Issue 5, 2011, pp. 1530-1536.

[2]. K. Z. Guyton, *et al*., Carcinogenicity of tetrachlorvinphos, parathion, malathion, diazinon, and glyphosate, International Agency for Research on Cancer Monograph Working Group, IARC, Lyon, France, *Lancet Oncology*, Vol. 16, Issue 5, 2015, pp. 490-491.

[3]. M. Enserink, P. J. Hines, S. N. Vignieri, N. S. Wigginton, J. S. Yeston, The Pesticide Paradox, *Science*, Vol. 341, Issue 6147, 2013, pp. 728-729.

[4]. J. Bajgar, Organophosphates/nerve agent poisoning: mechanism of action, diagnosis, prophylaxis, and treatment, *Advances in Clinical Chemistry*, Vol. 38, 2004, pp. 151-216.

[5]. M. Pohanka, K. Musilek, K. Kuca, Progress of biosensors based on cholinesterase inhibition, *Current Medicinal Chemistry,* Vol. 16, Issue 14, 2009, pp. 1790-1798.

[6]. F. Tortora, F. Febbraio, G. Manco, E. Porzio, Development of new bioreceptors for pesticides detection, in *Proceedings of the 7th International Conference on Sensors Engineering and Electronics Instrumentation Advances (SEIA' 2021),* 22-24 September 2021, Palma de Mallorca, Spain, pp. 101-102.

[7]. N. W. M. Van Buren, A. G. H. Mariën, H. H. W. Velthuis, The effectiveness of systemic agents used to control the mite, Varroa jacobsoni, in colonies of the honey bee, Apis mellifera, depends on food distribution patterns, *Apidologie,* Vol. 24, Issue 1, 1993, pp. 33-43.

[8]. M. I. Smodiš Škerl, V. Kmecl, A. Gregorc, Exposure to Pesticides at Sublethal Level and Their Distribution Within a Honey Bee (*Apis mellifera*) Colony, *Bulletin of Environmental Contamination and Toxicology,* Vol. 85, 2010, pp. 125-128.

[9]. C. A. Mullin, *et al*., High levels of miticides and agrochemicals in North American apiaries: implications for honey bee health, *PloS ONE,* 2010.

[10]. CFR: Appendix A to Part 355—The List of Extremely Hazardous Substances and Their Threshold Planning Quantities, (PDF) (July 1, 2008 ed.). Government Printing Office. Archived from the original (PDF) on February 25, 2012. Retrieved October 29, 2011.

[11]. P. Carullo, G. P. Cetrangolo, L. Mandrich, G. Manco, F. Febbraio, Fluorescence Spectroscopy Approaches for the Development of a Real-Time Organophosphate Detection System Using an Enzymatic Sensor, *Sensors,* Vol. 15, 2015, pp. 3932-3951.

[12]. P. Carullo, M. Chino, G. P. Cetrangolo, S. Terreri, A. Lombardi, G. Manco, A. Cimmino, F. Febbraio, Direct detection of organophosphate compounds in water by a fluorescence-based biosensing device, *Sensors and Actuators B: Chemistry,* Vol. 255, 2018, pp. 3257-3266.

Sensors & Transducers, Vol. 253, Issue 6, November 2021, pp. 23-30

www.sensorsportal.com

Sensors & Transducers

Published by IFSA Publishing, S. L., 2021
http://www.sensorsportal.com

Foreign Body Detection in Frozen Food by Dual Energy X-Ray Transmission

*** Christine BAUER, Rebecca WAGNER and Johannes LEISNER**
Fraunhofer IIS, Fraunhofer Institute for Integrated Circuits IIS, Division Development Center X-Ray Technology, Flugplatzstr, 75, 90768 Fürth, Germany
Tel.: +49911580617663, fax: +49911580617299
E-mail: christine.bauer@iis.fraunhofer.de

Received: 22 October 2021 /Accepted: 23 November 2021 /Published: 30 November 2021

Abstract: Foreign bodies of different types may find their way unnoticed into frozen food during processing or while packing. These contaminating objects show a great variety of materials, but consist most likely of glass, plastics, metal or (fish-) bone. The contaminants may cause considerable product recalls because of their hazardous nature for the consumer, leading to suffocation or shortness of breath. Eventually, the reputation of the respective manufacturer is long-termed harmed. Dual energy X-ray transmission is a powerful tool in non-destructive testing and thus may provide a solution to detect different foreign bodies in frozen food. We used this method for studying different frozen foods like mixed berries or vegetables and convenience food contaminated with aluminum, synthetic bones, Teflon, steel and glass test objects of different diameters in the range from 0.3 mm to 10 mm. The study shows that dual energy X-ray transmission is suitable to detect certain contaminants in frozen food while it reveals weakness in reliably discovering plastics. A general limitation of a contaminants' size that can be detected with this method is the spatial resolution of the measurement setup. Especially in highly heterogeneous environments, dual energy outperforms conventional X-ray transmission.

Keywords: Dual energy, X-ray, X-ray transmission, Basis material decomposition, Food safety, Food contaminants, Foreign body detection.

1. Introduction

Today many producers have to call back their products due to appearing safety issues or product defects. On the German market, the number of product recalls increases every year (except in 2017) resulting in a record high of 297 in 2019 (Fig. 1) [1].

In that year, almost one third of the product recalls, namely 90, occurred in the food sector followed by defective toys and faulty leisure items or sporting goods (Fig. 2).

The main reasons for the food producers to recall their products are faulty packaging and foreign bodies, which entered the product prior to packaging. The product recalls are mainly triggered by incidences of suffocation or shortness of breath (40 %) [1].

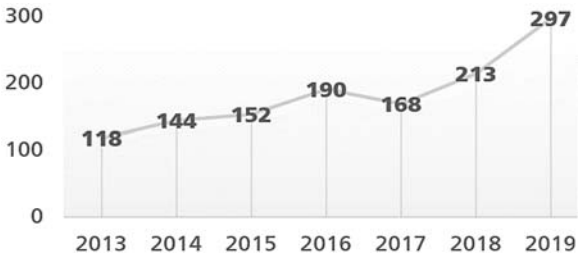

Fig. 1. Number of published product recalls on the German market from 2013 to 2019 (data from [1]).

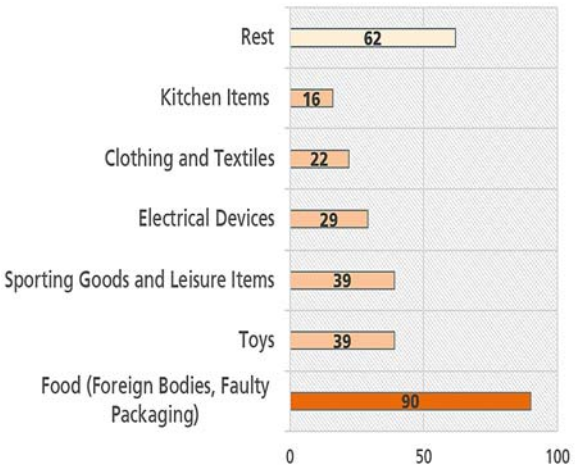

Fig. 2. Number of product recalls per product group on the German market in 2019 (data from [1]).

It can be said that product recalls are not only very costly (around \$ 10^6 for a company [2]), but also lead to the elimination of high amounts of goods (e.g. food, electronic devices) and a long-lasting harm of the manufacturer's reputation.

There are various technologies to find foreign bodies in products. Optical methods are limited to the objects' surface, while others rely on electrical conductivity or magnetism [3]. In comparison to technologies like metal detection, X-ray transmission (XRT) is not limited to one kind of material and may find foreign bodies like plastics, glass, bone fragments and metals also in packed food [4]. Additionally, there are also several approaches to detect defects in fruits with X-ray imaging [5, 6].

Nevertheless, XRT has its limits, as objects with low attenuation are hard to find especially in heterogeneous environments, i.e. environments that lead to a considerable spatial fluctuation of X-ray attenuation. An approach that is used not only in modern medicine but also in various security applications and non-destructive testing (NDT) is the use of dual energy methods [7]. They are based on the material specific variation in transmission and absorption of X-rays with energy. Unlike standard XRT that only allows separating materials based on their X-ray attenuation, dual energy X-ray transmission (DE-XRT) is capable of acquiring quantitative information like the areal density [8] or the mass percentage of measured materials [9]. Thereby the areal density image of one material is mostly independent of the other material.

Applications which need an NDT technology for quality control and involve highly heterogeneous 'background material' like food are prone to be solved with a DE-XRT approach. In this paper, we present several examples for the detection of foreign bodies in food using DE-XRT. While we will concentrate on frozen food for the remainder of this publication, the method was also successfully applied to food types like nuts, wafer treats and tofu balls [10].

2. Experimental

2.1. Sample Materials

In total, five samples were chosen to test various types of frozen food including convenience food. The studied samples were:

- A frozen paella, a rice dish with vegetables, seafood, salmon and chicken,
- Whole frozen strawberries,
- A frozen berry mix containing strawberries, blackberries, raspberries, redcurrants, blueberries and sour cherries,
- Frozen Asian styled fried vegetables with cauliflower, savoy, carrots, onion, pepper, ginger and soy sauce,
- Frozen buttered vegetables, namely peas, carrots, corn and cauliflower.

Eight test cards including five calibrated spherical test objects of different diameters *d* made by RONDOTEST® [11] were used (Table 1, Fig. 3 right), namely aluminum, glass, steel (AISI 304) and Teflon (PTFE). Two additional test cards contained cubic test bodies of synthetic bone with edge length *d* (Table 1, Fig. 3 left).

Table 1. Used test cards with their respective materials and thicknesses.

Material	Thickness [mm]				
	d_1	d_2	d_3	d_4	d_5
Aluminum	0.5	0.8	1.0	1.2	1.5
Aluminum	2.0	2.5	3.0	3.5	4.0
Synth. Bone	2.0	3.0	4.0	5.0	6.0
Synth. Bone	6.0	7.0	8.0	9.0	10.0
Glass	0.5	0.8	1.0	1.2	1.5
Glass	1.5	2.0	2.5	3.0	3.5
Steel AISI304	0.3	0.4	0.5	0.6	0.8
Steel AISI304	0.6	0.8	1.0	1.2	1.5
Teflon PTFE	2.0	2.5	3.0	3.5	4.0
Teflon PTFE	4.0	5.0	6.0	7.0	8.0

Fig. 3. Left: Test card for synthetic bone with five cubic test bodies (6 mm to 10 mm). Right: Test card for glass with five spherical test bodies (1.5 mm to 3.5 mm).

2.2. Dual Energy X-ray Transmission

The measurements were performed using a drawer system moving between a high-power X-ray source (Comet MXR225/HP11) as well as a dual energy line detector (Fig. 4). The used detector was a Hamamatsu C10800-09FCM-C with a pixel pitch of 0.4 mm. As

the detector was placed directly below the drawer, the X-ray images are obtained with minimal magnification. Therefore, the pixel pitch of the detector corresponds directly to the spatial resolution of the images. The detector consists of two sensor layers, so that it records two images (high- and low-energy) simultaneously at different X-ray energies. The samples were placed in the drawer, which moved with a speed of approx. 170 mm/s. The scans were carried out with 100 kV, 5 mA and an exposure time of 2.67 ms per recorded line.

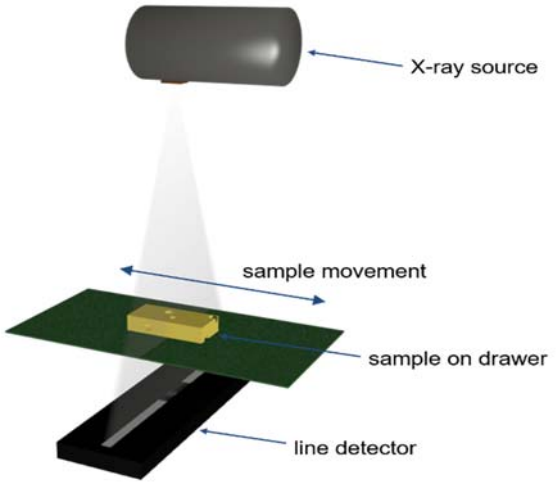

Fig. 4. Scheme of the measurement procedure: the sample is moved between the X-ray source and the dual energy line detector (adapted from [12] published under license CC BY 4.0).

For analysis of the data, basis material decomposition (BMD) was applied [8, 9, 13]. This method utilizes the energy dependence of X-ray attenuation. It requires two images of a sample, recorded with different spectral parameters, i.e. one with lower energy (LE) and one with higher energy (HE). This can be achieved by different means. For the work presented in this paper, a dual energy detector was used. Other options would be the use of different filters or changing the tube voltage. Applying BMD to two spectrally different XRT images, yields the areal densities p_l and p_h of two materials l (light) and h (heavy) that have to be chosen by the user. The areal density is defined as the materials density multiplied by its thickness [12] (Fig. 5).

BMD is based on the Lambert-Beer law, which describes the intensity I behind an object with areal density p and mass attenuation coefficient μ':

$$I = I_0 e^{-p\mu'}, \tag{1}$$

where I_0 is the non-attenuated intensity.

This approach includes the attenuation of X-rays by Compton scattering as well as photoelectric absorption. Typical laboratory X-ray sources are not monochromatic. Thus, the detected non-attenuated intensity is given by:

$$I_0 = \int dE\, S(E) * D(E), \tag{2}$$

with $D(E)$ being the detector efficiency and $S(E)$ the spectrum emitted by the source. Using Eq. 1 and Eq. 2 leads to:

$$I = \int dE\ * e^{-p\mu'(E)} * S(E) * D(E) \tag{3}$$

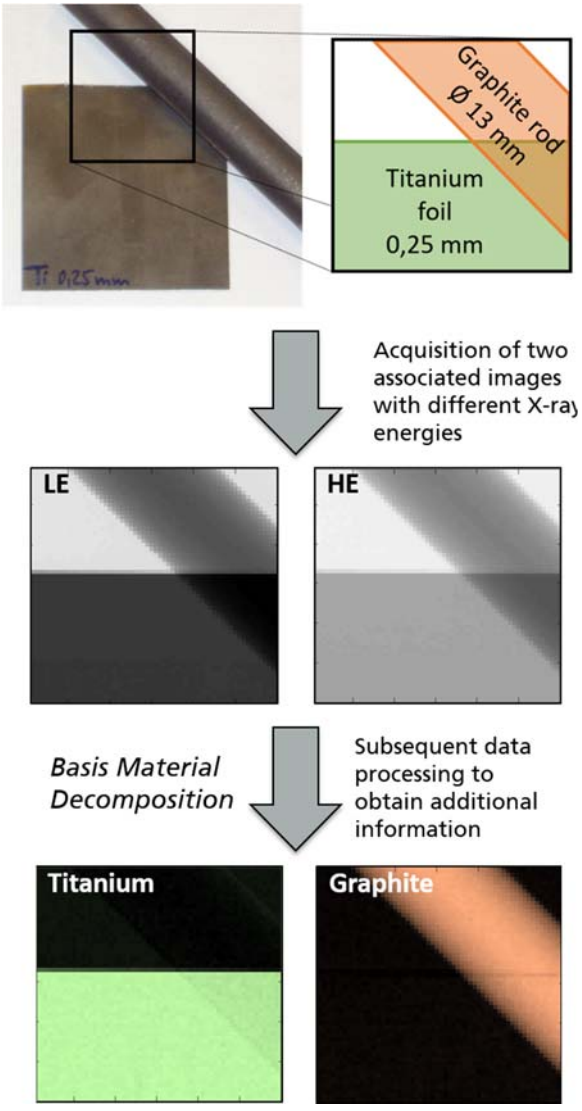

Fig. 5. Scheme of the data processing procedure exemplified with two pure materials: a graphite rod overlapping a titanium foil (adapted from [14]).

The attenuation coefficients of different materials sum up when more than one material is penetrated. Acquiring two measurements at different spectral parameters leads to a set of two equations. This set describes the extinction of the same material composition at different spectral parameters k, leading to:

$$I_k = \int dE\ * e^{-\sum p_j \mu'_j(E)} * S_k(E) * D(E) \tag{4}$$

with *j* being the index of the material. To solve this set of equations, the product $D(E) * S(E)$ has to be known.

It can be obtained either by simulation or measurement techniques [15]. As the mass attenuation coefficient μ' is tabulated, equation (4) allows to compute the areal densities p_1 and p_2 of two chosen materials by solving the set of equations given by two measurements with different X-ray energies.

The investigated samples, especially the food, are chemically complex materials, so their X-ray attenuation properties are determined by their effective atomic number Z_{eff}. It can be calculated by using

$$Z_{eff}^{k} = \frac{\sum_i z_i^k \rho_i}{\sum_i \rho_i}, \text{ with } k \approx 3, \quad (5)$$

where Z_i are the constituent's atomic numbers and ρ_i the constituents' partial chemical densities [16].

Here, the light material was the background, i.e. the food with an assumed effective atomic number around 7.5 that was adjusted to the respective object (for details see 3. Results). The heavy material was aluminum (effective atomic number of 13), glass (Z_{eff} = 11.6), PTFE (Z_{eff} = 10), steel (Z_{eff} = 26) or bone (Z_{eff} = 11.3).

3. Results

Fig. 6 shows the high-energy image of the frozen Asian styled fried vegetables including the ten aluminum test objects. The five aluminum beads of the first card with a diameter between 2.0 mm and 4.0 mm are difficult to see with the bare eye and can hardly be discriminated from the food. The beads of the second card with smaller diameter (0.5 mm to 1.5 mm) are completely unrecognizable.

In this case, detection by automated image processing would be very challenging. The overlapping diverse vegetables create a highly heterogeneous absorption image that is almost impossible to be segmented, especially with automatic thresholding methods.

The resulting BMD image for aluminum is shown in Fig. 7. It displays the areal density of aluminum. The frozen vegetables (Z_{eff} = 7.7) vanish almost completely in this image and some of the test bodies can clearly be seen. Here, the segmentation of the aluminum beads is feasible for the bigger spheres (2.0 mm to 4.0 mm). For the smaller beads only 1.0, 1.2 and 1.5 mm can be detected.

With a line tracker of five pixels in width (Fig. 8) the grey value in the HE X-ray projection and the areal density of the test bodies were obtained (Fig. 9 for the bigger spheres and Fig. 10 for the smaller beads).

The line profiles show fluctuations of the grey values due to the heterogeneous structure of the food. As a result, even the bigger test bodies can hardly be identified based on their grey values. However, the areal density line profiles show that there is sufficient contrast between background and several of the test bodies. Of the five bigger beads (Fig. 9), four could be identified by applying a threshold, while the smallest one with d = 2 mm is harder to distinguish from noise.

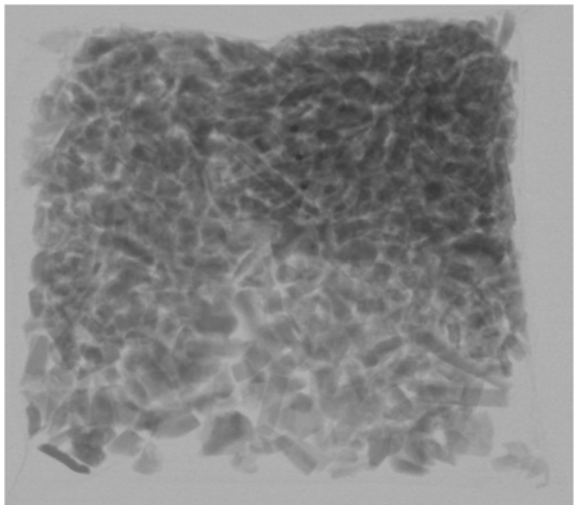

Fig. 6. High-energy XRT image of frozen Asian styled fried vegetables contaminated with aluminum.

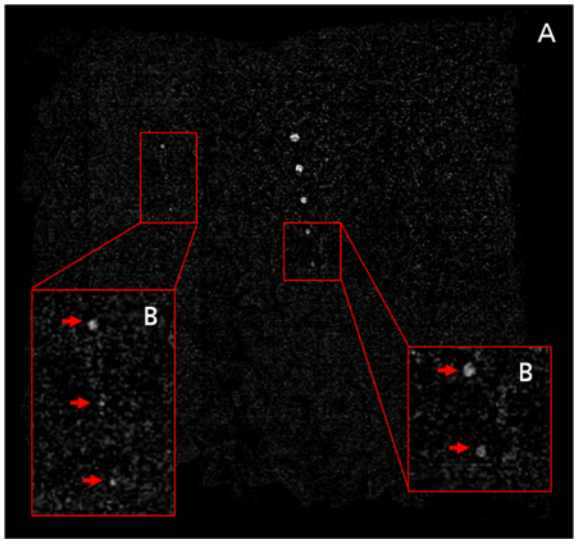

Fig. 7. A: Areal density image of aluminum. The five bigger contaminants are clearly visible, while only three of the smaller ones can be detected. The frozen vegetables ('background') disappear. B: Magnification of 2.5 of the framed areas in A (red). Red arrows indicate the approximate location of the aluminum beads.

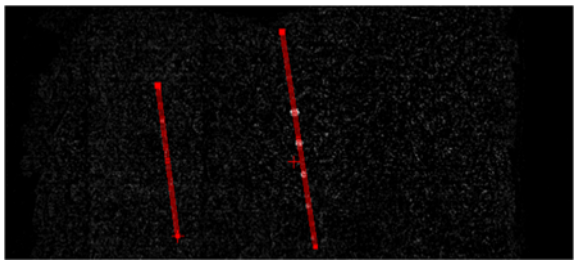

Fig. 8. Areal density image of aluminum with two line trackers of five pixels in width.

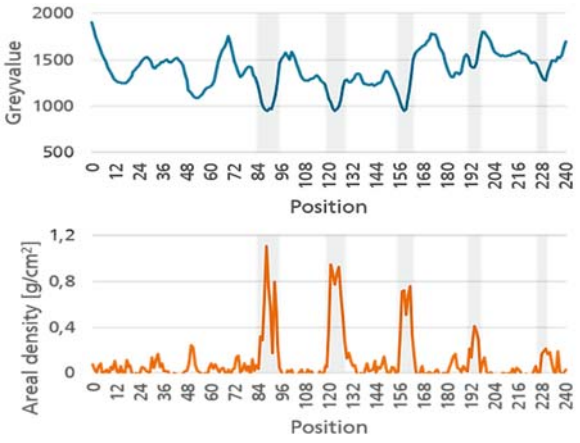

Fig. 9. Grey value in the HE X-ray projection (blue) and areal density (orange) of the five bigger test bodies (2.0 mm to 4.0 mm) acquired by a line tracker of five pixel in size. Grey pillars indicate the approximate positions of the five beads.

Fig. 10. Grey value in the HE X-ray projection (blue) and areal density (orange) of three of the five smaller test bodies (1.0, 1.2 and 1.5 mm) acquired by a line tracker of five pixel in size. Grey pillars indicate the approximate positions of the three beads.

Of the smaller set (Fig. 10), only the biggest test body with d = 1.5 mm could be discriminated using a simple threshold. This example illustrates that for edge cases the ability to detect contaminants may depend on their local surrounding. For instance, similar sized foreign bodies may be detected at one location, while at a different position a longer penetration length through the surrounding food can increase noise and thus prevent a detection. Especially for these edge cases, the situation could be improved by applying further image processing methods. Morphological operators like opening could be used to remove noise but retain the 'clusters' of bright pixels caused by the foreign bodies. Also the use of artificial intelligence for de-noising of images attracts more and more interest [17].

In Fig. 11 the high-energy XRT image of the frozen paella can be seen. The image is very heterogeneous due to the rice and vegetable pieces. Big squared darker regions trace back to pieces of salmon, more round spots to pieces of chicken. The five bigger test objects of synthetic bone (6.0 mm to 10.0 mm) are visible, while the smaller ones (2.0 mm to 6.0 mm) are very difficult to see. In contrast, the cubes of synthetic bone can be seen easily in the areal density image (Fig. 12), because the 'background', i.e. the paella (Z_{eff} = 7.5), vanishes almost completely.

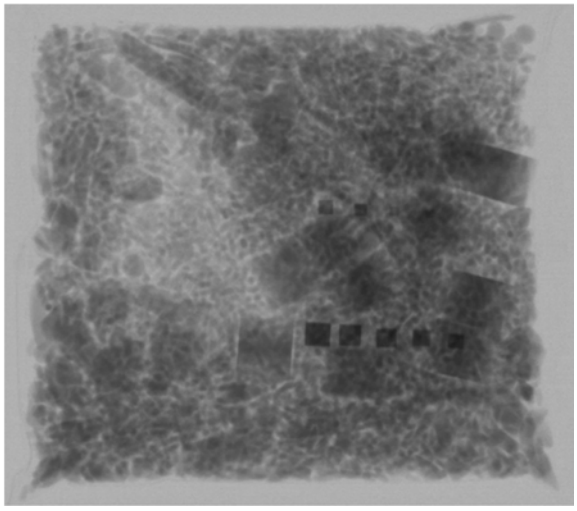

Fig. 11. High-energy XRT image of frozen paella contaminated with synthetic bones.

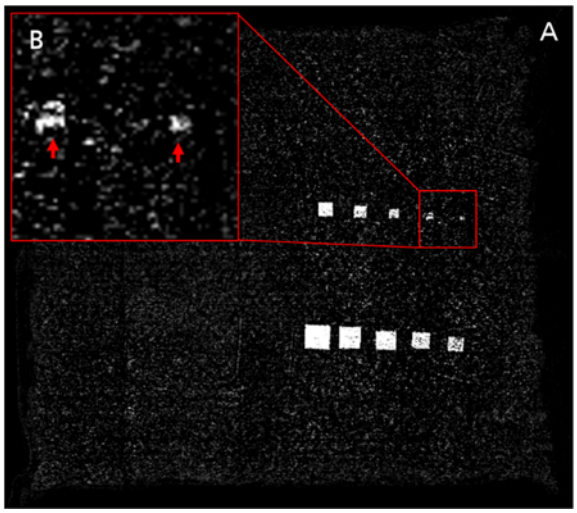

Fig. 12. A: Areal density image of (synthetic) bone. All ten contaminants are clearly visible. The frozen convenience food disappears. B: Magnification of 4 of the framed area in A (red). Red arrows indicate the approximate location of the synthetic bone cubes.

The strawberries in Fig. 13 are contaminated with glass beads. The images of three beads are overlapping the strawberries while two are placed (close) beside them. Due to the overlap, it is not possible to distinguish all the glass spheres from the food by thresholding.

In the BMD image (Fig. 14) this problem does not occur: all five bigger glass beads (1.5 mm to 3.5 mm) can be detected because the strawberries disappear (Z_{eff} = 7.4). The smaller beads (0.5 mm to 1.2 mm) of the second test card are beyond the detection limit. The biggest one of this set is equal in diameter to the smallest bead of the first test card (d = 1.5 mm). Nevertheless, it can not be detected as it is situated on top of a strawberry. In contrast, the equally sized bead in the first test card is not overlapping any fruit. Again, this shows the dependence of the detection limit for edge cases on the environment.

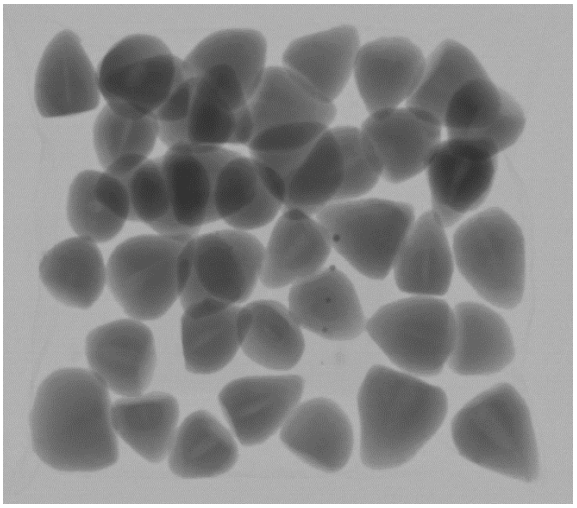

Fig. 13. High-energy XRT image of frozen strawberries contaminated with glass.

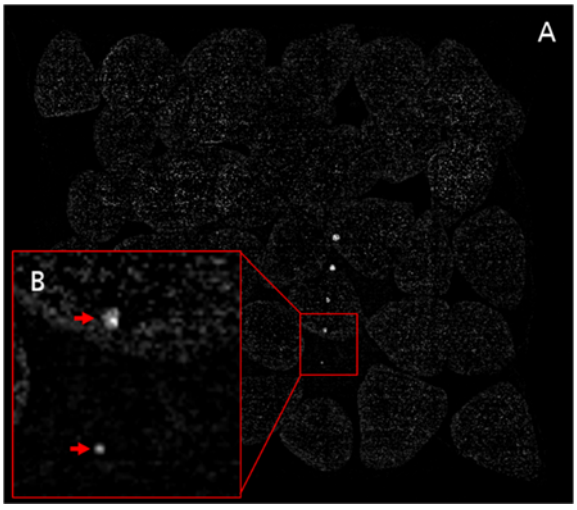

Fig. 14. A: Areal density image of glass. The five bigger contaminants are clearly visible. The frozen strawberries disappear. B: Magnification of 4 of the framed area in A (red). Red arrows indicate the approximate location of the glass beads.

In Fig. 15 the highly heterogeneous high-energy XRT image of frozen buttered vegetables can be seen. This sample is contaminated with steel test bodies with a diameter between 0.3 mm and 1.5 mm. Some of them can be seen with the bare eye but despite the high contrast in the effective atomic numbers (Z_{eff} = 7.2 and Z = 26) only the three biggest ones can be detected easily by segmentation.

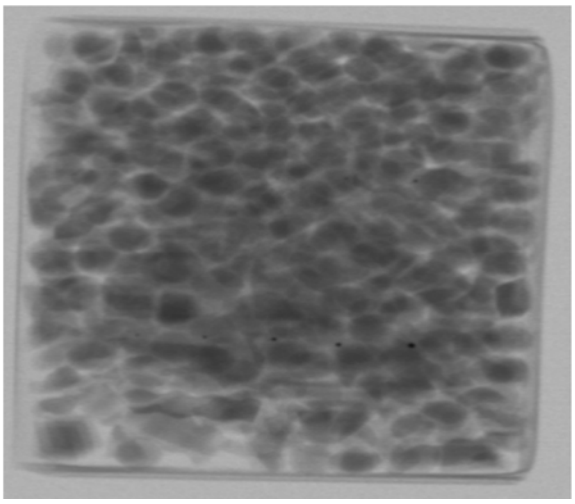

Fig. 15. High-energy XRT image of frozen buttered vegetables contaminated with steel AISI 304.

In the areal density image (Fig. 16), the steel contaminants can be seen much easier against the vanishing 'background'. While the four biggest spheres of the first test card (0.8 mm to 1.5 mm) can be detected easily by applying a threshold, the smallest one (0.6 mm) needs some image processing to be segmented.

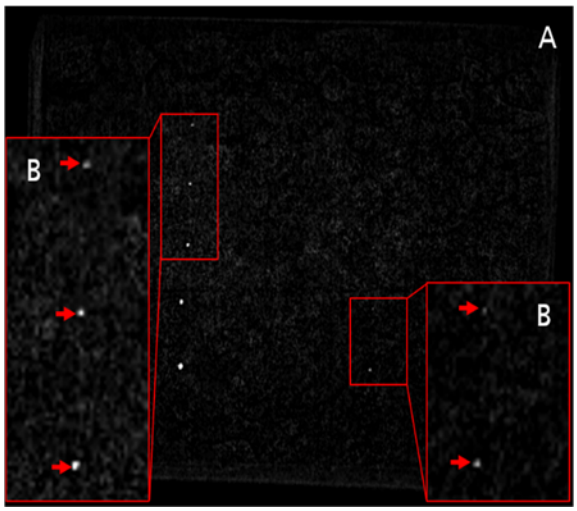

Fig. 16. A: Areal density image of steel. The four bigger contaminants are clearly visible. The smallest bead of the card with the bigger contaminants and the biggest bead of the card with the smaller contaminants are visible with some effort. The frozen vegetables disappear. B: Magnification of 2.5 of the framed areas in A (red). Red arrows indicate the approximate location of the steel beads.

The same is true for the biggest sphere of the second test card (0.8 mm). The second biggest bead of

this card is hardly visible with the bare eye and thus marks the detection limit. Again, the reason for the difference in detectability for equally sized beads in the two test cards is their different location on the sample.

Fig. 17 displays a high energy XRT image of a berry mix that has been contaminated with PTFE. The test objects can not be recognized based on their grey values. This is expected as their effective atomic number (Z_{eff} = 10) is very close to food (Z_{eff} = 7.5) due to their chemical composition (carbon and fluor). Thus, they hardly increase the attenuation in comparison to food.

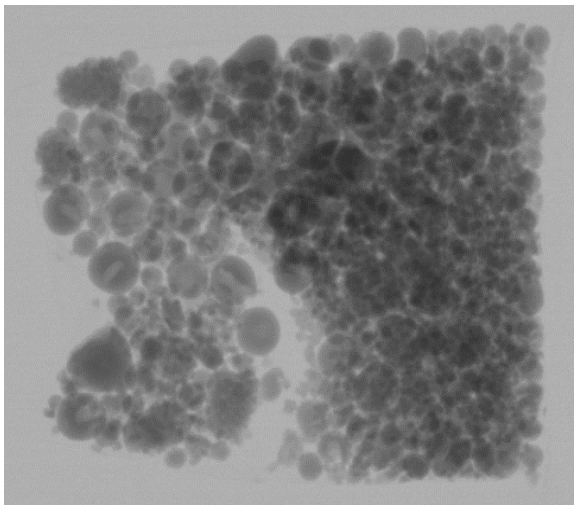

Fig. 17. High-energy XRT image of a frozen berry mix contaminated with PTFE.

The chemical similarity of PTFE and food also prevents the successful application of the BMD. In the areal density image shown in Fig. 18, the test objects can not be distinguished from noise. The two largest spheres (d = 7 mm and d = 8 mm) are visible only as a cluster of bright pixels with grey values similar to noise.

The line profiles in Fig. 19 show how low the contrast between the PTFE beads and their respective background is in both high-energy and areal density image.

4. Conclusion

Table 2 shows a summary of the results obtained for the various test specimen used as contaminants in the presented experiments. Their respective detectability is illustrated by different colors. Green means that a detection is possible by simply applying a threshold. Red indicates that finding the foreign body is not possible either because its size is below the spatial resolution limit of the detector and/or because its (effective) atomic number is too close to that of the food. Sizes labeled in yellow are edge cases. Here, thresholding is not sufficient to find the foreign bodies.

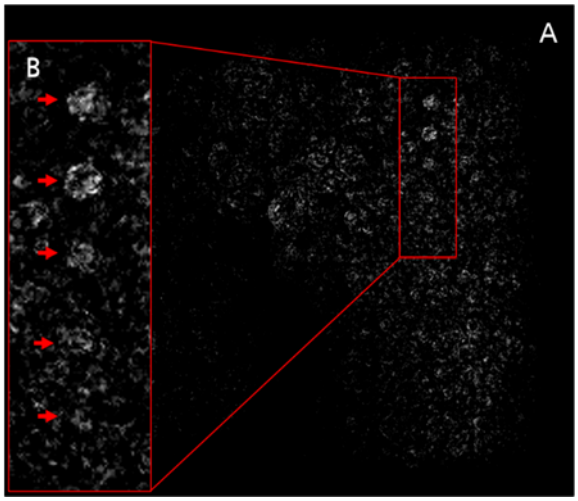

Fig. 18. A: Areal density image of PTFE. The contaminants are difficult to see. B: Magnification of 2.5 of the framed area in A (red). Red arrows indicate the approximate location of the PTFE beads.

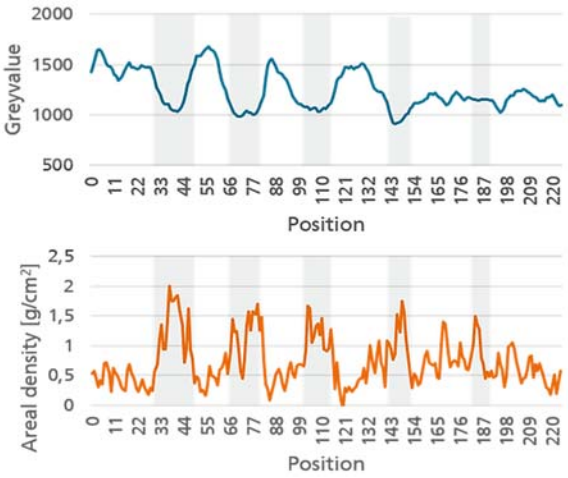

Fig. 19. Grey value in the HE X-ray projection (blue) and areal density (orange) of the five bigger test bodies (4.0 mm to 8.0 mm) acquired by a line tracker of five pixel in width. Grey pillars indicate the approximate positions of the five beads.

However, further image processing methods can allow their detection. Especially for foreign bodies with sizes marked in yellow, detectability may depend on the thickness of the food at their respective location.

The results of this study show that DE-XRT is a suitable and powerful method for detecting contaminants of various materials in frozen foods of different types. It can be shown that DE-XRT is able to detect aluminum, synthetic bone, glass and steel even in highly structured and heterogeneous environments like mixed berries or convenience food where standard XRT is likely to fail. The dual energy algorithm works the better, the more different the (effective) atomic numbers of the materials to be discriminated are. Thus, detecting PTFE in food was very difficult.

Table 2. Used test cards with their respective materials and thicknesses and their detectability for the presented approach and setup.

Material	Thickness [mm]				
	d_1	d_2	d_3	d_4	d_5
Aluminum	0.5	0.8	1.0	1.2	1.5
Aluminum	2.0	2.5	3.0	3.5	4.0
Synth. Bone	2.0	3.0	4.0	5.0	6.0
Synth. Bone	6.0	7.0	8.0	9.0	10.0
Glass	0.5	0.8	1.0	1.2	1.5
Glass	1.5	2.0	2.5	3.0	3.5
Steel AISI304	0.3	0.4	0.5	0.6	0.8
Steel AISI304	0.6	0.8	1.0	1.2	1.5
Teflon PTFE	2.0	2.5	3.0	3.5	4.0
Teflon PTFE	4.0	5.0	6.0	7.0	8.0

Detectable
Detection Limit
Not Possible

In general, the method is not only limited by the contrast in the atomic numbers, but also by the spatial resolution of the imaging system. For a reliable detection, contaminants have to be discriminated from the noise in the respective areal density images. Especially for contaminants with lower contrast to food, the size in the XRT images should preferably be at least 3 px x 3 px. This limits the detection of contaminants to sizes of $d \gtrsim 1.2\,\mathrm{mm}$, although a large difference in the atomic numbers might relax that criterion to some extent.

Acknowledgements

The authors would like to thank Hamamatsu Photonics Deutschland GmbH for providing the measurement setup at the Fraunhofer Development Center X-ray Technology in Fürth/ Germany.

References

[1]. Website of Bundesamt für Arbeitsschutz und Arbeitsmedizin (https://www.baua.de/DE/Angebote/Publikationen/Berichte/ProdSG-2020.html).

[2]. Website of Food Safety Magazin (https://www.food-safety.com/articles/2542-recall-the-food-industrys-biggest-threat-to-profitability?v=preview).

[3]. M. Graves, A. Smith, B. Batchelor, Approaches to foreign body detection in foods, *Food Science and Technology*, Vol. 9, Issue 1, 1998, pp. 21-27.

[4]. R. P. Haff, N. Toyofuku, X-ray detection and contaminants in the food industry, *Sensing and Instrumentation for Food Quality and Safety,* Vol. 2, Issue 4, 2008, pp. 262-273.

[5]. T. F. Schatzki, R. P. Haff, R. Young, I. Can, L.-C. Le, N. Toyofuku, Defect detection in apples by means of X-ray imaging, *Transactions of the American Society of Agricultural Engineers,* Vol. 40, Issue 5, 1997, pp. 1407-1415.

[6]. R. P. Haff, D. C. Slaughter, Y. Sarig, A. Kader, X-ray assessment of translucency in pineapple, *Journal of Food Processing and Preservation*, Vol. 30, Issue 5, 2006, pp. 527-533.

[7]. R. E. Alvarez, A. Macovsk, Energy-selective reconstructions in X-ray computerised tomography, *Physics in Medicine and Biology,* Vol. 21, Issue 5, 1976, pp. 733-744.

[8]. M. Firsching, J. Mühlbauer, A. Mäurer, F. Nachtrab, N. Uhlmann, Quantitative sorting using dual energy X-ray transmission imaging, in *Proceedings of the Conference on Optical Characterization of Materials (OCM'2013)*, Karlsruhe, Germany, 6-7 March 2013, pp. 259-264.

[9]. M. Firsching, J. Lucic, A. Ennen, N. Uhlmann, Concentration determination for sorting applications using dual energy X-ray transmission imaging, in *Proceedings of the Conference on Optical Characterization of Materials (OCM'2017),* Karlsruhe, Germany, 22-23 March 2017, pp. 65-74.

[10]. C. Bauer, R. Wagner, J. Leisner, Potential of Dual Energy X-ray Transmission on Food Safety, in *Proceedings of the 7th International Conference on Sensors and Electronics Instrumentation Advances (SEIA'2021),* Palma de Mallorca, Mallorca (Balearic Islands), Spain, 22-24 September 2021, pp. 90-93.

[11]. Rondotest Website (https://rondotest.de/).

[12]. C. Bauer, R. Wagner, B. Orberger, M. Firsching, A. Ennen, C. Garcia Pina, C. Wagner, M. Honarmand, G. Nabatian, I. Monsef, Potential of Dual and Multi Energy XRT and CT Analyses on Iron Formations, *Sensors,* Vol. 21, Issue 7, 2021, pp. 2455.

[13]. M. Firsching, F. Nachtrab, N. Uhlmann, R. Hanke, Multi□Energy X□ray Imaging as a Quantitative Method for Materials Characterization, *Advanced Materials*, Vol. 23, Issue 22□23, 2011, pp. 2655-2656.

[14]. M. Firsching, J. Mühlbauer, F. Nachtrab, A. Jobst, Basis Material Decomposition – a Quantitative X-ray Imaging Method and its Application in Industrial Sorting, in *Proceedings of the Symposium on Digital Industrial Radiology and Computed Tomography (DIR'2021)*, Berlin, Germany, 20-22 June 2011.

[15]. E. Y. Sidky, L. Yu, X. Pan, Y. Zou, M. Vannier, A robust method of X-ray source spectrum estimation from transmission measurements: Demonstrated in computer simulated, scatter-free transmission data, *Journal of Applied Physics,* Vol. 97, Issue 12, 2005, pp. 124701-1 – 124701-11.

[16]. B. Heismann, J. Leppert, K. Stierstorfer, Density and atomic number measurements with spectral X-ray attenuation method, *Journal of Applied Physics,* Vol. 94, Issue 3, 2003, pp. 2073-2079.

[17] A. E. Ilesanmi, T. O. Ilesanmi, Methods for image denoising using convolutional neural network: a review, *Complex & Intelligent Systems*, 2021, pp. 1-20.

Sensors & Transducers, Vol. 253, Issue 6, November 2021, pp. 31-36

www.sensorsportal.com

Sensors & Transducers

Published by IFSA Publishing, S. L., 2021
http://www.sensorsportal.com

A Model for Electrical Properties Measurement of Graphene-based Composites with an Open-ended Coaxial Probe Technique

[1, *] Hind BAKLI, [2] Mohamed MOUALHI and [3] Mourad MAKHLOUF

[1] Laboratory of Electronics and Electrical Systems Engineering,
BP 48 Cherchell, Tipaza, 42006, Algeria
[2] Laboratory of Software Implementation and Validation, Algiers, 16000, Algeria
[3] Laboratory of Combustion, Detonation and Ballistic, BP 48 Cherchell, Tipaza, 42006, Algeria
[1] Tel.: + 213671614893
E-mail: baklih@yahoo.com

Received: 29 October 2021 /Accepted: 28 November 2021 /Published: 30 November 2021

Abstract: Electrical properties measurement of graphene-based composite materials in the frequency range 1-18 GHz is proposed in this paper. These materials have been prepared by adding different mass percentages ranging from 1 to 40 % of graphene to PVC. The measurement setup is based on the association of an open-ended coaxial probe and a vector network analyzer. A modeling based on a modified calibration one port model and capacitive approach is proposed to relate the measured microwave signal to the complex permittivity and conductivity of the material under test.

Keywords: Dielectric permittivity, Microwave characterization, Open-ended coaxial probe, Graphene, Polymer.

1. Introduction

Excellent properties of graphene-based polymer composites [1-2] including high flexibility, good thermal and electrical conductivity, low temperature processing conditions, and simple fabrication process have allowed its use in different applications such as electronic devices, electromagnetic shielding, photovoltaic cells, sensors, supercapacitors, Li ion batteries, protective coating, biomedical applications and water purification, etc. [3-5].

The knowledge of electrical properties of conductive polymer materials is required when using these materials, especially at high frequencies. These properties have been measured using different microwave techniques including resonant cavities, open-ended coaxial probe, waveguides and transmission lines based methods. Since it has the advantages of being non-destructive to the materials, the ability of wideband measurement and the easiness of sample preparation, the open-ended coaxial probe technique is the most commonly used one. This technique consists of placing an open-ended coaxial transmission line in contact with a sample so that the electrical fields around the end of the probe interact with the sample under test and measuring changes in the reflection coefficient affected by the electromagnetic properties of the sample [6-7].

In this paper, a calibration model based on a modified conventional one port calibration and lumped elements models is proposed to retrieve the graphene-based composite materials electrical properties from measured reflection coefficient measured when using an open-ended coaxial probe.

The modified one port calibration model is used to relate the measured reflection coefficient to the one at the aperture-plane of the probe. Capacitive approach is used to model the open-ended aperture admittance when a composite material is set to the probe contact and thus to relate the reflection coefficient at the aperture-plane to the electrical properties of the material. The permittivity and conductivity of the prepared graphene-based composite materials are experimentally extracted using the proposed model in the frequency range 1-10 GHz.

2. Modeling of the Probe-sample Interaction

When the open-ended probe is placed in the vicinity of the sample, its electromagnetic properties affect the detection system parameters. A modeling of the structure under investigation which represents the interaction between the probe and the sample is then used to retrieve the electromagnetic properties of the sample from the parameters measured by the detection system.

In this work, a homemade open-ended probe (the inner diameter of the outer conductor is D= 4.1 mm and the diameter of the inner conductor is d= 1.3 mm) is used to characterize different graphene-based composite materials. We present in Fig. 1 the simulated distribution at a frequency of 2.45 GHz of the electrical field at the end of the coaxial probe. From this figure, we notice that the field is concentrated around the open end of the probe. Thus, lumped elements model can be used to describe the interaction between the open-ended probe and the material under test. Thus, the aperture admittance can be modeled as two parallel capacitors, as illustrated in Fig. 2.

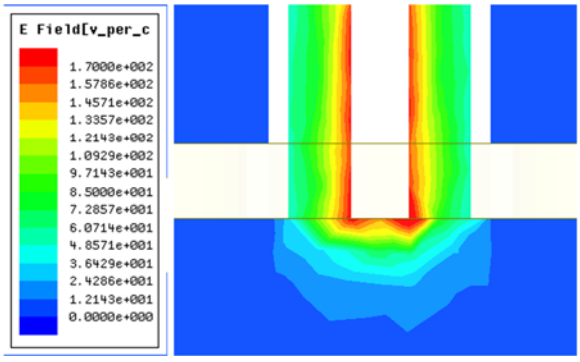

Fig. 1. HFSS™ simulation of the electric field magnitude - F = 2.45 GHz.

From this model, the open-ended aperture admittance Y_{MUT} can be obtained by the following equation

$$Y_{MUT} = j\omega\left(C_f + \varepsilon_r C_0\right), \quad (1)$$

where C_f is the capacitance determined by fringing-fields effects inside the probe, C_0 is the capacitance that is related to the microwave coupling between the probe and the composite material, ω is the angular frequency and ε_r is the complex permittivity of the material.

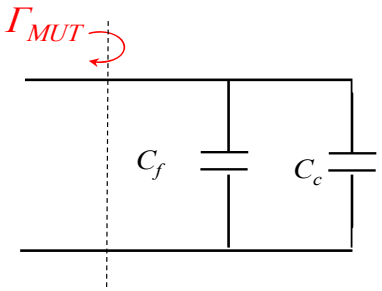

Fig. 2. Lumped elements model for open-ended coaxial probe.

3. Experimental Procedure

3.1. Sample Preparation

In this work, we used graphite (as electrodes) and electrolyte baths (electrochemical cell) composed of sulfuric acid and water for the exfoliation process. Thus, we performed the electrochemical exfoliation of graphite in sulfuric acid to obtain high quality and large-area graphene thin sheets.

In a typical electrochemical process, a two-electrode system has been used in which a graphite rod acts as an anode and another rod acts as a cathode in a solution of sulfuric acid H_2SO_4. The electrolyte consisted of 100 ml of aqueous solution with a volume ratio of 1/4 of H_2SO_4 and H_2O. A DC voltage of 10 V was applied until the total consumption of the graphite rod which was converted to graphene sheets within 1.5 hours.

The aqueous solution of graphene ink was centrifuged and washed several times with distilled water after sonication for half an hour. Finally, our graphene is dried for 24 hours at 333 °K. After drying our graphene electrochemically (GE) this material is subjected to a microwave treatment for 30 seconds to separate the sheets of graphene from each other, the latter will be named (GE-MW).

Polyvinyl chloride (PVC SIGMA ALDRICH, 98 %) was used as a polymer matrix. A mass of graphene ranging from 0 % to 40 % was dispersed for 15 minutes in an emulsion of dibutyl sebaceate (DBS) under ultrasonic vibration. A mass of PVC was added to the mixture (G/DBS) and finally, the mixture was subjected to a heat treatment at 423 °K for 1 h 30. In order to study the effect of loads on the properties of PVC, a series of nanocomposites were made and the elaborate compositions are summarized in Table 1.

The experimental part of this research includes the preparation of the raw material, graphene (G) with electrochemical method.

Table 1. Compositions and mass fractions of engineered nanocomposites.

PVC	DBS	G
45 %	55 %	0 %
45 %	54 %	1 %
45 %	53 %	2 %
45 %	51 %	4 %
45 %	49 %	6 %
45 %	47 %	8%
45 %	45 %	10 %
45 %	35 %	20 %
45 %	25 %	30 %
45 %	15 %	40 %

Our samples were analyzed with X-ray diffraction. This technique allows the analysis of the crystalline phases contained in a sample. Information on its microstructure (size of the crystallites, micro stresses) can also be extracted.

X-ray diffraction is based on the recording of a diffractogram, which allows you to identify / quantify the phases, calculate the crystallographic parameters and determine the average size of the crystallites by different methods (Scherrer, Williamson-Hall).

Our samples were analyzed using a D8 Advance Eco diffractogram (Bruker) operating with a copper tube ($\lambda = 1.54$Å)

The X-ray spectrum of the graphite powder (Fig. 3) shows the hexagonal structure according to the (002) orientation, as revealed by the single peak at $2\theta = 25°$ which corresponds to a spacing of about 3, 4 A° between the graphite planes.

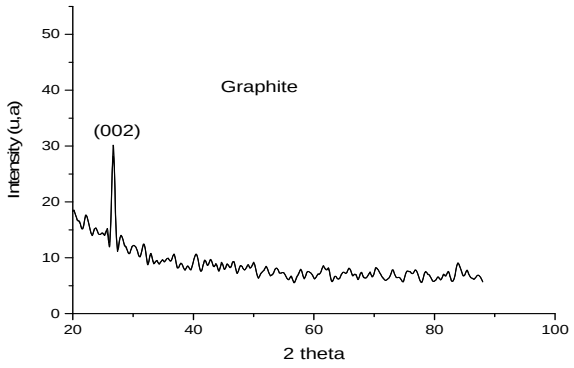

Fig. 3. XRD patterns of Graphite XRD.

The graphene X-ray spectra (GE-MW) (Fig. 4) show the absence of the diffraction peak in comparison with graphite ($2\theta = 26.4°$). This indicates the removal of the periodicity in the structure of Graphene exfoliated. In fact, the increase in the inter-spacing following the oxidation of the graphite comes from the intercalation of the oxygen-containing groups between the layers of the graphite, thus weakening the van der Waals forces between the layers, which allow an exfoliation easy via sonification in an aqueous medium.

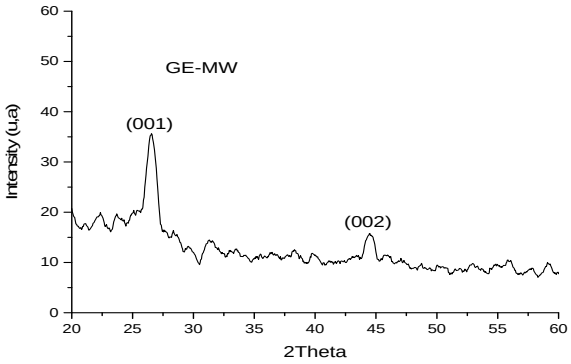

Fig. 4. XRD patterns of GE and GE-MW.

We present in Fig. 5 the scanning electron microscopy image of the graphene used in composites samples. This image shows the dynamic form of graphene and confirms the existence of homogeneity in the microscopic structure.

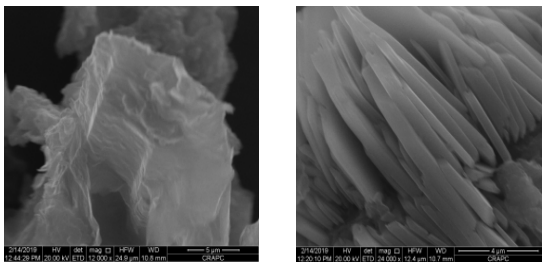

Fig. 5. SEM image of graphene.

3.2. Experimental Set-up

We present in Fig. 6, the experimental set-up based on the association of the homemade open-ended coaxial probe and a vector network analyzer (Rhode & Schwarz ZVL6). The power has been fixed to 0 dBm and then SOL calibration has been performed.

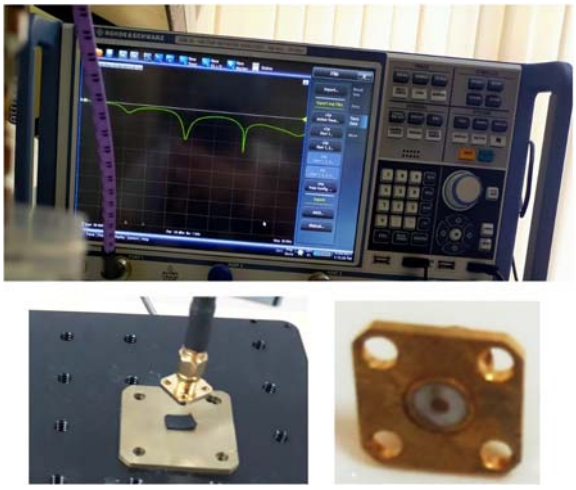

Fig. 6. Experimental set-up.

4. Calibration Model

To relate the measured reflection coefficient Γ to the desired reflection coefficient referenced at the end of the coaxial probe Γ_{MUT}, a phenomenological flow graph using a modified one-port calibration model (Fig. 7) is shown below.

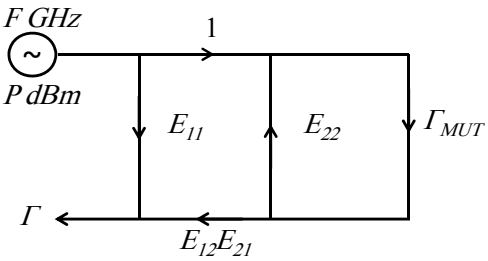

Fig. 7. Signal flow graph for a one port calibration model.

From this graph, the measured reflection coefficient Γ can be obtained by the following equation

$$\Gamma = E_{11} + \frac{E_{12}E_{21}\Gamma_{MUT}}{1 - E_{22}\Gamma_{MUT}}, \quad (2)$$

where the complex terms E11, E12 E21 and E22 are calibration coefficients that correspond respectively to the directivity, source match and reflection tracking errors. The reflection coefficient Γ_{MUT} at the end of the probe is given by

$$\Gamma_{MUT} = \frac{Y_{MUT}(\varepsilon_r) - Y_0}{Y_{MUT}(\varepsilon_r) + Y_0}, Y_0 = 1/Z_0, Z_0 = 50\Omega, \quad (3)$$

where Y_{MUT} is the open-ended aperture admittance.

By combining the relations (1) to (3), we can get the following equation

$$\Gamma = \frac{A_2 + A_3\varepsilon_r}{A_1 - \varepsilon_r}, \quad (4)$$

where A_1, A_2 and A_3 are three frequency-dependent complex constants, related to E_{11}, E_{12} E_{21}, E_{22}, Z_0, C_f and C_0.

Three materials (air, PTFE and de-ionized water) selected for calibration with known permittivity are used to solve the system (4) and determine A_1, A_2 and A_3. The material permittivity is then retrieved by inverting equation (4) for the different composites. The sample permittivity is given by $\varepsilon_r = \varepsilon' - j\varepsilon''$, where ε' and ε'' are the real and imaginary parts of dielectric permittivity. The conductivity of the composite material is then calculated using

$$\sigma = 2\pi f \varepsilon_0 \varepsilon'', \quad (5)$$

where f is the frequency of measurement.

5. Results and Discussions

We present in Fig. 8, the different magnitude spectra of the reflection coefficient for the different composite materials prepared by adding to PVC different concentrations of graphene ranging from 1 to 40 %.

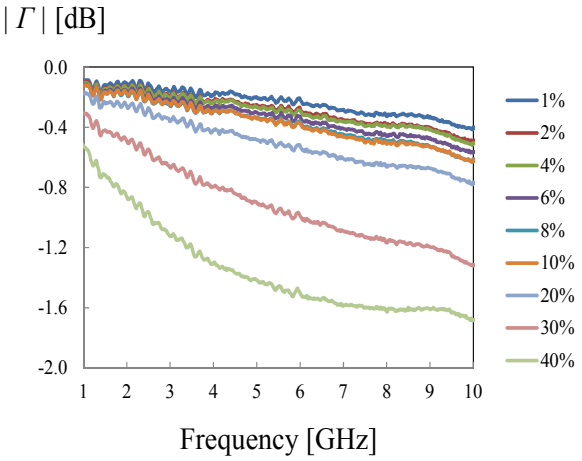

Fig. 8. Measured magnitude spectra of the reflection coefficient for different G-PVC composite materials.

It is clearly shown in Fig.8 that the different G-PVC composite materials are well differentiated by means of reflection coefficient magnitude. When the graphene concentration increases, the reflection coefficient magnitude decreases. This can be attributed to the electron motion hysteresis under an alternating electromagnetic field which induces additional polarization relaxation processes that increase the microwave absorption.

We present in Fig. 9 the experimentally determined dielectric permittivity for the different graphene-based composites. It is retrieved that as the concentration of graphene increases, the particles interaction within the polymer matrix increases. This results in higher polarization, and hence, a higher dielectric constant.

We present in Fig. 10 the measured real and imaginary parts of the permittivity and the conductivity at a test frequency of 2.45 GHz for the different samples.

From these graphs, it can be seen that for the different graphene-based composites, when the graphene concentration increases, the real and imaginary parts of permittivity and the conductivity increase. In fact, by increasing the graphene concentration, the interaction of the particles within the matrix goes up. The average polarization correlated to a cluster of particles is more robust than an individual particle due to the improved inclusion dimensions of the composite and thus a larger interfacial area, resulting in a higher average polarization, and thus a larger contribution to the dielectric properties and conductivity.

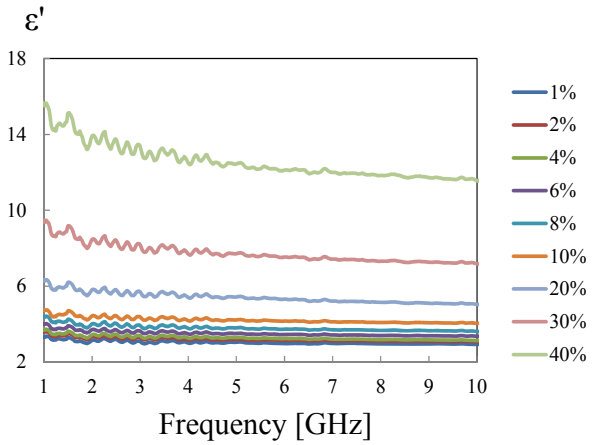

(a)

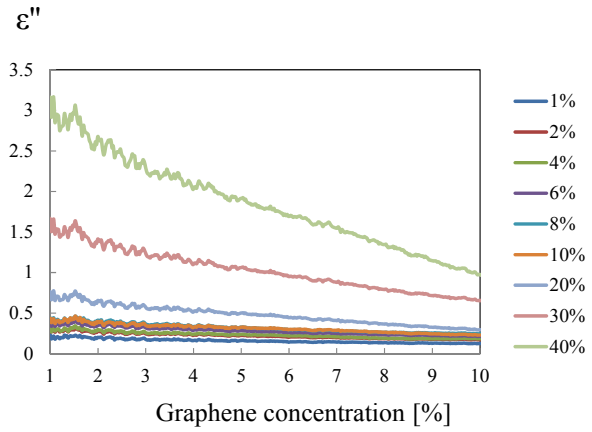

(b)

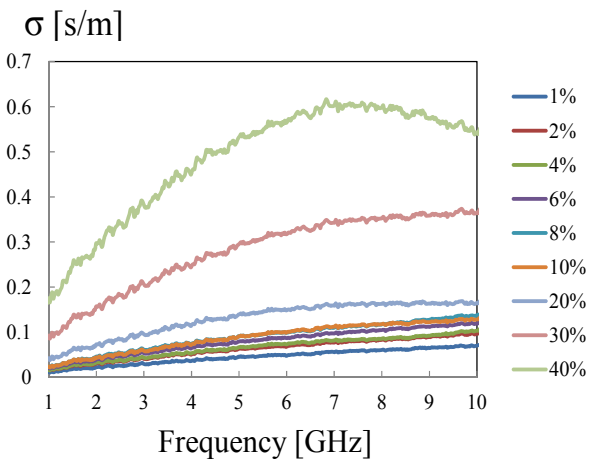

(c)

Fig. 9. Measured electrical properties of G-PVC composite materials. (a, b) real and imaginary parts of permittivity, (c) conductivity.

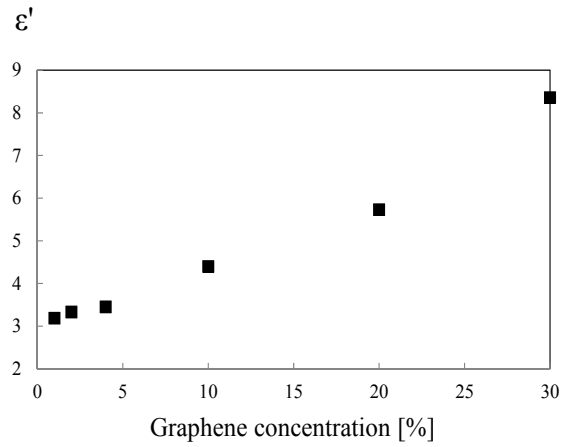

(a)

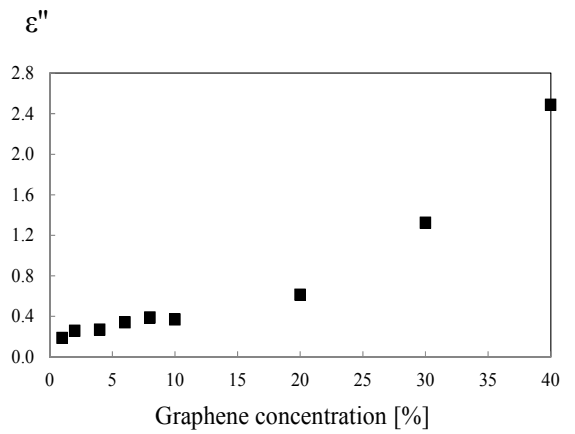

(b)

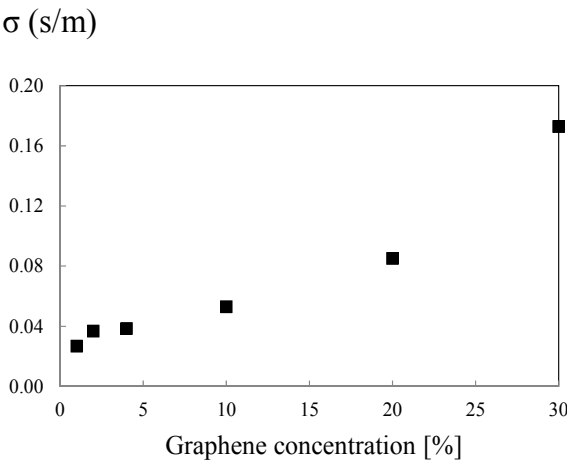

(c)

Fig. 10. Measured electrical properties of G-PVC composite materials. (a, b) real and imaginary parts of dielectric permittivity, (c) conductivity.

6. Conclusions

Electrical properties of Graphene-based composites have been experimentally determined using open-ended coaxial probe in the frequency band ranging from 1-10 GHz. A lumped elements model has been used to describe the interaction between the open-ended probe and the material under test. A modified one-port model has been proposed to relate the measured reflection coefficient to the electrical properties of the material. The results obtained show the capacity of the proposed method for wide-band characterization of composite materials.

Acknowledgements

Measurements have been done in the Signals and Systems Laboratory of the Institute of Electrical and Electronic Engineering, University M'hamed BOUGARA of Boumerdes, Algeria.

References

[1]. T. K. Das, S. Prusty, Graphene-Based Polymer Composites and Their Applications, *Polymer-Plastics Technology and Engineering*, Vol. 52, Issue 4, 2013, pp. 319-331.

[2]. X. Huang, C. Zhi, Y. Lin, H. Bao, G. Wu, P. Jiang, Y.-W. Mai, Thermal Conductivity of Graphene-based Polymer Nanocomposites, *Materials Science and Engineering: R: Reports*, Vol. 142, 2020, pp. 100577.

[3]. G. Wu, P. Tan, D. Wang, Z. Li, L. Peng, Y. Hu, C. Wang, W. Zhu, S. Chen, W. Chen, High-performance Supercapacitors based on Electrochemical-induced Vertical-aligned Carbon Nanotubes and Polyaniline Nanocomposite Electrodes, *Scientific Reports*, Vol. 7, Issue 1, 2017, pp. 1-8.

[4]. M. He, J. Jung, F. Qiu, Z. Lin, Graphene-based Transparent Flexible Electrodes for Polymer Solar Cells, *Journal of Materials Chemistry*, Vol. 22, Issue 46, 2012, pp. 24254.

[5]. W. Guo, J. Su, Y.-H. Li, L.-J. Wan, Y.-G. Guo, Nitroxide Radical Polymer/graphene Nanocomposite as an Improved Cathode Material for Rechargeable Lithium Batteries, *Electrochimica Acta*, Vol. 72, 2012, pp. 81-86.

[6]. H. Bakli, K. Haddadi, T. Lasri, Quantitative Determination of Small Dielectric and Loss Tangent Contrasts in Liquids, in *Proceedings of the on IEEE International Instrumentation and Measurement Technology Conference (I2MTC)*, Turin, Italy, 2017.

[7]. H. Bakli, M. Moualhi, M. Makhlouf, Electrical Properties Measurement of Graphene-based Composites using an Open-ended Coaxial Probe Technique, in *Proceedings of the 7th International Conference on Sensors and Electronic Instrumentation Advances (SEIA' 2021)*, Palma de Mallorca, Spain, 2021, pp. 72-75.

Sensors & Transducers, Vol. 253, Issue 6, November 2021, pp. 37-43

www.sensorsportal.com

Sensors & Transducers

Published by IFSA Publishing, S. L., 2021
http://www.sensorsportal.com

The Optimization Function of Lognormal Distribution on the Airborne Particle Counter Channel

Juan Yang
School of Electrical and Information Engineering, Jinling Institute of Technology,
Nanjing 211169, China
Tel.: 18913805443
E-mail: yangjuan@jit.edu.cn

Received: 4 October 2021 /Accepted: 26 November 2021 /Published: 30 November 2021

Abstract: With the increase of fog and haze weather, people pay more and more attention to the pollution of the suspended particulates in the air. And, the development of science and technology requires high cleanliness make the measurement of the aerosol and the improvement of the instrument become more important. In this paper, on the basis of analyzing the typical particle size measurement process by the light scattering method, the statistical model of light scattering particle's random measurement is established. Meanwhile, the theoretical deduction indicates that the statistical distribution function in the light scattering random signal measurements meets a lognormal distribution function with the natural number as the independent variable. The experiment results manifest that the introduction of the lognormal distribution into the counting channel optimization of the measurement instruments 1) Saves the counting channels, 2) Expands the sensor's measurement range by 1/3 and enhances the instrument's ability to distinguish the small particles.

Keywords: Airborne particle counter, Lognormal distribution, Counting channel, Optimization.

1. Introduction

In recent years, as the effect of fog haze weather, environment detection, especially PM2.5 monitoring problem, receives more and more people's attention. Therefore, the research on method and the instrument for analyzing and accurately quantitative measuring pollution is of great significance. So far, people have developed many measuring methods based on different principle [1-4]. Among which, light scattering as a kind of important method, because of fast measuring speed, high precision and good repeatability, as well as got the favor of scientists and engineers. Consequently, it has been widely used in particle parameters measurement [5, 6].

In the detection system based on the principle of light scattering, the particles correspond to the discrete signal group of light scattering random voltage pulse. The system put the amplitude of the pulse signal as a basis for determining the size of particle [7, 8]. The particle morphology's irregular, light intensity's inhomogeneity of photosensitive area and other factors cause different photosensitive area, even if the same particles' signal amplitude and width, which indicates the randomness [9, 10]. So, different particles' counting distribution of signal amplitude (width) has a certain overlap [11], which leads to a certain measurement error.

This article analyzes the process of particle size's measurement based on typical light scattering method, and a statistical model of random measurement is established. Combined with double parameters analysis method of random pulse signal, it is found that the light scattering signal characteristics quantity

meet logarithmic normal distribution with natural number as the independent variable and have statistical self-similarity. Based on which, the lognormal distribution is applied to the channel optimization of measuring instrument. The experimental results show that the optimization can save the counting channel, expand the measurement range, and enhance the instrument's ability to distinguish small particle size of particles.

2. Statistical Distribution of Standard Particle Light Scattering Signal

2.1. Optical Particle Counter Measurement System

The experimental device is shown in Fig. 1. Aerosol flows through an optical sensing volume, and the light scattered by a single particle is collected and focused by a mirror in the angular range. And then, the light signal is converted to an electrical pulse by a photo-detector. Through pre-amplification and multichannel collection, the voltage pulse of the particle is obtained by a computer. The experimental apparatus and measuring environment are easy to be realized, and the measuring accuracy could be guaranteed. Besides, the system can obtain enough data with good repeatability. The higher the accuracy of the measuring system in recording signals, the larger sample size is measured in unit time. So the statistical characteristics of random signals will be more obvious.

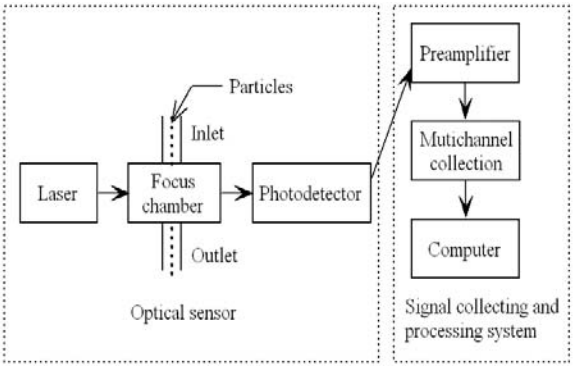

Fig. 1. Schematic diagram of optical particle counter system.

As a result of the discrete degree of standard particle's size is small, the same size's standard particle signal amplitude distribution reflects the nature of the interaction between particles and sensors. Therefore, the statistical distribution of measurement results reflect the randomness of sensor noise, photosensitive area in-homogeneity, the instability of scattered light collecting efficiency, etc. The PG-100 type particle generator of PMS Company is adopted in experiment, and diluted standard particle emulsion is put after spraying into measurement system. And, the large flow semiconductor new airborne particle counter is used to measure standard particles with different size. The mainly technical parameters are listed as follows. A collimated continuous laser beam (808 nm, 50 mW) is used as the light source, and the photosensitive area is about 0.5 mm×1 mm×8 mm. The reversed biased voltage is set to be 12 V, dark current is no more than 10^{-9}A. The sampling rate is 28.3 L/min, the maximal range of voltage is 5 V which is divided into 2048 counting channels. The maximal signal sampling rate is 20 MHz (the corresponding time-accuracy $\Delta\tau$=0.05 μs), continuously sampled data of signal is up to 1×10^7, a 1000 level ultra-clean room is the measuring environment only for measuring the background noise.

2.2. The Characteristic Parameter of the Random Signal for Standard Particle

It is well known that the output signal of photo-electricity in airborne particle counter corresponds to a time series $f(t)$. However, the signal in actually experimental measurement could not be continuous, which can be attributed to the experimental results have a certain time accuracy Δt. In other words, $f(t)$ must be written as $f(k \cdot \Delta t)$ which is a natural number sequence. Taking a reference value f_0 to process the experimental results, a subset $V(t) = f(t) - f_0 > 0$ can be gotten. The elements, which have continuous time sequence in subset $V(t)$, compose a pulse structure with the amplitude and width are defined as V and τ respectively, as shown in Fig. 2.

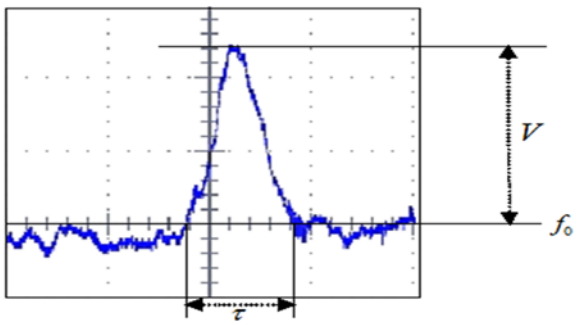

Fig. 2. Sketch map of the pulse structure.

On the basis of the above analysis, a new characteristic subset $A(V,\tau)$ composed by random pulse signal sequences can be used to describe the random signal group $f(t)$ which is dealt with f_0. Owing to the universality of $f(t)$, this signal

processing method has universal significance, where Δt and ΔV represent the characteristics of the measurement devices, while V and τ are the characteristic parameters of the pulse signal. Once the parameter group f_0, $\Delta\tau$ and ΔV are given, the physical parameters of the signal subset $\{A(V,\tau)\}$ can be described by the natural numbers. That is, a set of natural numbers (l_τ, l_V) can used to establish the statistical mapping form of the signal subset $\{A(V,\tau)\}$:

$$\begin{aligned} l_\tau &= \left\lfloor \frac{\tau_i}{\Delta\tau} - 1 \right\rfloor \quad l_\tau \in \left(1,2,\cdots,L_\tau = \frac{\tau_M}{\Delta\tau} - 1\right) \\ l_V &= \left\lceil \frac{V_i}{\Delta V} \right\rceil \qquad l_V \in \left(1,2,\cdots,L_V = \frac{V_M}{\Delta V}\right) \end{aligned} \tag{1}$$

According to the size sequence of the observation character values l_τ (or l_V), the characteristic subset and the statistically descriptive form can be established. Let N denotes the total number of $\{A(V,\tau)\}$, while $\Delta N(l_\tau)$ and $\Delta N(l_V)$ denote the pulse numbers of $\{A(V,\tau|\tau \in l_\tau \Delta\tau)\}$ and $\{A(V|V \in l_V \Delta V, \tau)\}$ respectively. Hence, the pulse counting distribution functions of characteristic subset can be expressed as:

$$\begin{aligned} p(l_\tau) &\equiv \frac{\Delta N(l_\tau)}{N} = \frac{N_{l_\tau}}{N} > 0 \\ q(l_V) &\equiv \frac{\Delta N(l_V)}{N} = \frac{N_{l_V}}{N} > 0 \end{aligned} \tag{2}$$

Considering the knowledge of the statistics, the distribution functions $p(l_\tau)$ and $q(l_V)$ will tend to steady values when the sample's number of subsets satisfies $1 \ll \Delta N(l_\tau), and\ \Delta N(l_V) \ll N$ in actual measurement.

2.3. Standard Particle Light Scattering Signal Statistical Distribution Law

The statistical distribution functions of aerosol's pulse signals $q(l_V)$ and $p(l_\tau)$ are the projection that measure results are l_V and l_τ in the same environment, which means that they must have the same nature. So, if the nature of the random effect is not changed, the type of the one-dimensional statistical distribution function related this nature will be unchanged. Based on this, we can conclude that one-dimensional distribution functions $q(l_V)$ and $p(l_\tau)$ have the similarity because they reflect the common characteristics of the random effect. According to the theory and calculation analysis, reasonable control the influence of random factors on the measurement results in the process of measuring can improve the performance of the sensor. By using the improved new laser airborne particle counter sensor, the statistical distributions of random scattering pulse signal produced by several kinds of standard particle (PSL) with the diameters are 0.38 μm, 0.499 μm, 0.6 μm, 0.8 μm and 0.99 μm are measured. The amplitude counting distributions are shown in Fig. 3 by the dotted line, and the x axis is counting channel value, while the y axis is statistical probability value.

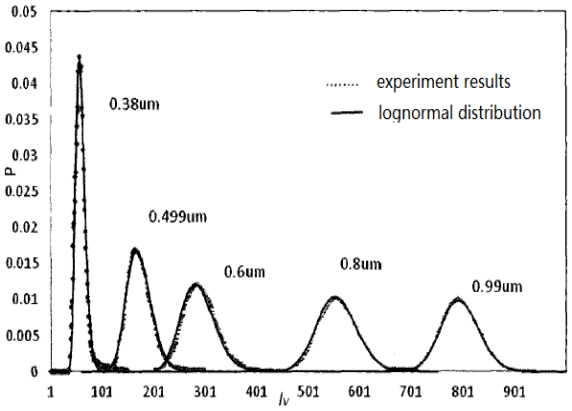

Fig. 3. Measured results and fitting distributions of standard particles.

As shown, the amplitude counting distributions have center asymmetry obviously. Besides, the nonlinearly similar characteristic between the different function sequences is quite well. According to the conclusions of the particle size, many research results shows that the lognormal distribution is a statistical distribution form with better effect for describing the particle parameters [12-14]. Therefore, we choose a statistical function with the form of log-normal distribution to fit the measured data. The fitting results can be seen as the sequence of solid lines in Fig. 3, and the corresponding equation satisfies:

$$q(l_V) = \frac{1}{\Omega \sigma_{\ln V} l_V} e^{-\frac{1}{2}\left(\frac{\ln l_V - \mu_{\ln V}}{\sigma_{\ln V}}\right)^2}, \tag{3}$$

where Ω is the normalized coefficient with a usual value $\sqrt{2\pi}$. It is easy to see, 5 standard particle pulse amplitude distribution curves meet logarithmic normal distribution, the fitting parameters such as Table 1 [15, 16].

Because the standard particles are sphere with the same material and surface structure, as well as the similar optical properties, the random effect of the measurement sensors for different size particles is similar. Hence, the geometric mean of the logarithmic normal distribution's fitting parameters is consistent with the certificated average diameter of standard particles.

Table 1. Statistic parameter values of the standard particle.

Sample	Total counting number N	Geometric mean $\mu_{\ln V}$	Geometric standard deviation $\sigma_{\ln V}$	Peak position l_V	Correlation coefficient *r*
0.38 *μm*	14802	4.54	0.25	57	0.93
0.499 *μm*	21010	5.14	0.24	154	0.97
0.6 *μm*	17886	5.60	0.22	280	0.98
0.8 *μm*	34062	6.32	0.28	553	0.98
0.99 *μm*	30223	7.20	0.25	790	0.94

3. The Nonlinear Transformation Statistical Invariance of Lognormal Distribution

The above experimental results show that the standard particle's random scattering pulse signal characteristic parameters obeys logarithmic normal distribution with the natural number as independent variable. It can be seen from Table 1, the fitting correlation coefficient is very high and the fitting effect is very good. Due to the similar random factors of different objects in the process of measurement, the pulse signal for the light scattering has statistical self-similarity law. For all characteristics statistical regularity obeys the lognormal distribution, a transformation rule can be found between the independent variables in theory, which makes experimental results of different characteristic parameters converge in geometry. Therefore, lognormal distribution should have self-similar properties of nonlinear transform unchanged. According to the differential mean value theorem, we can obtain [17]:

$$\begin{aligned} p_X(l_X)\triangle l_X &= \frac{\triangle l_X}{\Omega_X l_X \sigma_{X,\ln}} e^{-\frac{\left(\ln\frac{l_X}{l_{X,\mu}}\right)^2}{2\sigma_{X,\ln}^2}} \\ &= p_Y(l_Y)\triangle l_Y \\ &= \frac{e^{-\frac{\left(\ln\frac{l_Y}{l_{Y,\mu}}\right)^2}{2\sigma_{Y,\ln}^2}}}{\Omega_Y} \triangle\left\{\frac{1}{\sigma_{Y,\ln}}\ln\frac{l_Y}{l_{Y,\mu}}\right\} \end{aligned} \quad (4)$$

As expressed by Eq. (4), the independent variable of different characteristics parameters statistical distribution function can get the transformation relationship as:

$$l_Y = (bl_X)^{\frac{\sigma_{Y,\ln}}{\sigma_{X,\ln}}} \quad (5)$$

Obviously, the two independent variables, which have independent significance in the equation, could not take natural number sequence at the same time. When an argument is natural number sequence, another one is the non-integer count channel under the way of non-uniform division, which shows the nonlinear properties in the transformation. Thus, there can be thought a non-uniform channel divided way approach, so the different characteristics statistical distribution function curves coincide.

In further, transforming Eq. (5) to Eq. (4) by introducing scaling coefficient $Z = \Omega_X / \Omega_Y$ corresponding the transformation, we can have:

$$\begin{aligned} p_Y(l_Y)\triangle l_Y &= \frac{\triangle l_Y}{\Omega_Y l_Y \sigma_{Y,\ln}} e^{-\frac{\left(\ln\frac{l_Y}{l_{Y,\mu}}\right)^2}{2\sigma_{Y,\ln}^2}} \\ &= \frac{\Omega_X}{\Omega_Y}\cdot\frac{\triangle l_X}{\Omega_X l_X \sigma_{X,\ln}} e^{-\frac{\left(\ln l_X - \ln l_{X,\mu}\right)^2}{2\sigma_{X,\ln}^2}} \\ &= Z\cdot p_X(l_X)\triangle l_X \end{aligned}, \quad (6)$$

where the expression of b in the domain is:

$$b = e^{\frac{\sigma_{X,\ln}}{\sigma_{Y,\ln}}\ln l_{Y,\mu} - \ln l_{X,\mu}} = \frac{l_{Y,\mu}^{\frac{\sigma_{X,\ln}}{\sigma_{Y,\ln}}}}{l_X} \quad (7)$$

Thus, with two independent characteristic parameters amplitude V and width τ, when the statistical distribution function of different physical characteristic parameters has a lognormal distribution form, as:

$$\frac{V}{\Delta V}\cdot\frac{1}{l_{V,\mu}} = \left(\frac{\tau}{\Delta\tau}\cdot\frac{1}{l_{\tau,\mu}}\right)^{\frac{\sigma_{\ln V}}{\sigma_{\ln\tau}}}, \quad (8)$$

where $\alpha = \sigma_{\ln V} / \sigma_{\ln\tau}$ is the fractal dimension of characteristic parameter.

As a result, we get the statistical fractal self-similar nonlinear transformation formula of the different random independent physical characteristics. And, it is also known that the fractal dimension is non-integer

and only related to statistical discrete degree. From the above deduction, it can be seen that the statistical self-similar fractal nonlinear transformation relationship between different physical characteristics is only related to statistical parameters $l_{V,\mu}, l_{\tau,\mu}, \sigma_{\ln V}, \sigma_{\ln \tau}$, which reflects the constraint relationship between the overall nature and the internal statistical parameters of the random collection. Besides, the above deduction also reflects the equivalent position of different physical characteristics in the description of randomness for the random collection.

4. Airborne Particle Counter Counting Channel Optimization

Standard particle measurement corresponds to the sensor calibration process. When laser airborne particle counter is calibrated, standard particle voltage of the peak position is usually used to represent particle size. Then, we can gain the voltage corresponds to different size and achieve the effect of divided channel to count the particles' number. Fortunately, based on the research of the standard particle signal statistical distribution, looking for more and better optimal calibration method plays guiding role in improving sensors counting efficiency and particle size resolution.

From measurement results in Fig. 3, it can be found that this counter can separate different size particles completely, but there are defects of two aspects. First, the aerosol particle counter has a total of 2048 channels, but we only need about 900 channels to complete the calibration process of 5 kinds of standard particles, the rest of the channels are not used. Second, the particles of small size have the fewer counting channels, big size particles have the more counting channels. However, for the ultraclean environment of mainly used measuring instruments, people pay more attention to the distributions of small size particles.

Therefore, based on the nonlinear transform statistical invariance of the standard particle counting distribution curve, and the principle of guarantee adjacent size particles' resolution higher than 90 %, the sensor measurement channels for nonlinear are adjusted. Hereby, the magnification times of the small particle increase, and those of large size particles decreases. But no matter big or small size particles all can be accurately measured. For example, we can do nonlinear transformation based on power function in counting channel of Fig. 3 as Fig. 4.

Measured results and fitting distributions of standard particles by using the counting channel after the nonlinear transformation based on power function are shown in Fig. 5, the fitting parameters are such as those of Table 2 [15, 16]. Compared with Fig. 3, it can be found that different size particles' resolution remains the same after nonlinear transformation. Meanwhile, the statistical distribution of the standard particles is still in a form of logarithmic normal distribution. And, the statistical results of channel range originally in the range [1,901] now only 600 channels can be expressed, which means that we can get a wider range of particle size measurement within the inherent channel scope of the measuring instrument. That is to say, nonlinear transformation can increase measurement range of the instrument by 1/3.

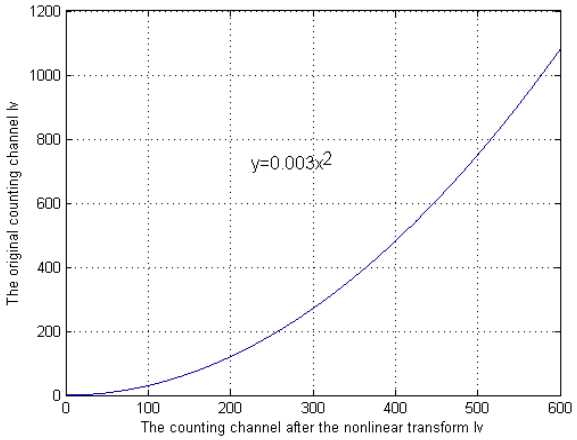

Fig. 4. The nonlinear transformation relation based on power function of counting channel.

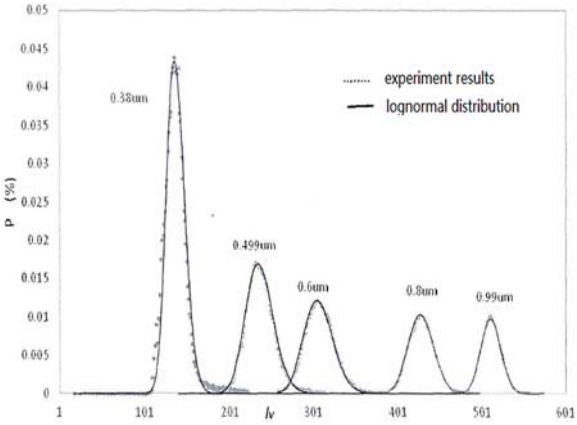

Fig. 5. Measured results and fitting distributions of standard particles after the nonlinear transformation.

Comparing Fig. 3 and Fig. 5, the form of particle statistical distributions has not any change after nonlinear transformation of counting channels, due to the properties of nonlinear transform invariant for lognormal distribution. Besides, the small particles' distribution curves move to the direction of big channels after transformation. The involved results manifest that this effects further improve the lower limit of the instrument as well as complete the distribution curves of the small particles and get more measurement details. In other words, this transformation can enhance the instrument's ability to distinguish small particle size.

Table 2. Statistic parameter values of the standard particle after the nonlinear transformation.

Sample	Total counting number N	Geometric mean $\mu_{\ln V}$	Geometric standard deviation $\sigma_{\ln V}$	Peak position l_V	Correlation coefficient r
0.38 *μm*	14802	4.54	0.25	138	0.92
0.499 *μm*	21010	5.14	0.24	227	0.94
0.6 *μm*	17886	5.60	0.22	306	0.97
0.8 *μm*	34062	6.32	0.28	429	0.97
0.99 *μm*	30223	7.20	0.25	513	0.96

5. Conclusion

The results with the airborne particle as the standard particle in counter are studied by theoretical analysis and experimental measurement. Experimental results show that the statistical distributions of light scattering random signal obey logarithmic normal distribution that regard natural number as the independent variable, under the condition of large sample and high precision. Further theoretical analysis results show that the logarithmic normal distribution has a good nonlinear transform statistical self-similarity. Based on this, the lognormal distribution is applied to the measuring instrument counting channels' optimization. The results manifest that the optimization can not only expand the measurement range of sensor by 1/3, and also promote the lower limit of the instrument, which can improve the instrument's ability to distinguish small particle size.

Acknowledgements

This work was funded by the National Natural Science Foundation of China (Grant No. 61302167) and the Scientific Research Startup Foundation of Jinling Institute of Technology (Grant No: jit-b-201111).

References

[1]. David C. Doughty, Steven C. Hill, Automated aerosol Raman spectrometer for semi-continuous sampling of atmospheric aerosol, *Journal of Quantitative Spectroscopy and Radiative Transfer*, Vol. 188, Issue 4, 2017, pp. 103-117.

[2]. Evgeny Kolesnikov, Gopalu Karunakaran, Anna Godymchuk, *et al*., Investigation of discharged aerosol nanoparticles during chemical precipitation and spray pyrolysis for developing safety measures in the nano research laboratory, *Ecotoxicology and Environmental Safety*, Vol. 139, Issue 5, 2017, pp. 116-123.

[3]. Benjamin Figgis, Ahmed Ennaoui, Bing Guo, Outdoor soiling microscope for measuring particle deposition and resuspension, *Solar Energy,* Vol. 137, Issue 12, 2016, pp. 158-164.

[4]. Lei Ding, Jin Bi Zhang, Hai Yang Zheng, A method of simultaneously measuring particle shape parameter and aerodynamic size, *Atmospheric Environment*, Vol. 139, Issue 8, 2016, pp. 87-97.

[5]. Gu Fang, Yang Juan, Bian Baomin, *et al*., Aerosol mass density algorithm based on average mass, *Acta Optica Sinica*, Vol. 27, Issue 9, 2007, pp. 1706-1710 (in Chinese).

[6]. Tian'en Wang, Jianqi Shen, Chengjun Lin, Iterative algorithm based on a combination of vector similarity *measure* and B-spline functions for particle analysis in forward scattering, *Optics & Laser Technology*, Vol. 91, Issue 7, 2017, pp. 13-21.

[7]. Stavros Amanatidis, M. Matti Maricq, Leonidas Ntziachristos, Measuring number, mass, and size of exhaust particles with diffusion chargers: The dual Pegasor Particle Sensor, *Journal of Aerosol Science*, Vol. 92, Issue 4, 2016, pp. 1-15.

[8]. Teimour Tajdari, Mohd Fua'ad Rahmat, Norhaliza Abdul Wahab, New technique to measure particle size using electrostatic sensor, *Journal of Electrostatics*, Vol. 72, Issue 2, 2014, pp. 120-128.

[9]. Yangang Lius, Peter H. Daum, The Effect of Refractive Index on Size Distributions and Light Scattering Coefficients Derived from Optical Particle Counters, *Journal of Aerosol Science*, Vol. 31, Issue 8, 2000, pp. 945-957.

[10]. Yang, Juan, Chen, Yun-Yun. The Aerosol Mass Measurement Based on the Two-parameter Mathematical Model in Optical Sensor, *Sensors & Transducers*, Vol. 175, Issue 7, July 2014, pp. 220-225.

[11]. R. Jaenicke, The optical particle counter: cross-sensitivity and coincidence, *Aerosol Science*, Vol. 30, Issue 7, 1972, pp. 95-111.

[12]. Lee K. W., Lee Y J, Han D. S., The Log-Normal Size Distribution Theory for Brownian Coagulation in the Low Knudsen Number Regime, *Journal of Colloid and Interface Science*, Vol. 188, Issue 4, 1997, pp. 486.

[13]. L. B. Kiss, J. Soderlund, G. A. Niklasson, C. G. Granqvist, The real origin of lognormal size distributions of nanoparticles in vapor growth processes, *Nanostructured Materials,* Vol. 12, 1999, pp. 327-332.

[14]. Kyu-Tae Park, Dongho Park, Sang-Gu Lee, Design and performance test of a multi-channel diffusion charger for real-time measurements of submicron aerosol particles having a unimodal log-normal size distribution, *Journal of Aerosol Science*, Vol. 40, Issue 10, 2009, pp. 858-867.

[15]. Yan Zhen Gang, Bian Bao Min, Wang Shou Yu, Analysis of random laser scattering pulse signals with lognormal distribution, *Chinese Physics B,* Vol. 22, Issue 6, 2013, pp. 246-256.

[16]. Yan Zhen Gang, Lin Ying Lu, Yang Juan, The distribution functions of characteristic quantities for

random noise signal of photodetector, *Acta Physica Sinica*, Vol. 61, Issue 20, 2012, pp. 200502 (in Chinese).
[17]. Yang Juan, Bian Baomin, Yan Zhengang, The Model of Two Parameters Statistical Fractal for Aerosol Scattering Pulse Signal, *Acta Physica Sinica*, Vol. 60, Issue 1, 2011, pp. 010508-1 – 010508-6 (in Chinese).

Sensors & Transducers, Vol. 253, Issue 6, November 2021, pp. 44-46

www.sensorsportal.com

Sensors & Transducers

Published by IFSA Publishing, S. L., 2021
http://www.sensorsportal.com

Short Message

Wearable Smart Sensor Ring to Monitor the Severity of Hand Tremor

[1, *] Ashok BATRA, [1] James SAMPSON, [1] Mohan AGGARWAL, [2, 3] Ashok VASEASHTA and [4] Kunal GROVER

[1] Materials Science Group, Department of Physics, Chemistry, and Mathematics
Alabama A&M University, Normal (Huntsville), AL 35762, USA
[2] International Clean Water Institute, Manassas, VA 20112, USA
[3] Biomedical Engineering and Nanotechnologies Institute, Riga Technical University, Riga, LV-1658, Latvia
[4] Henry Ford Health System - Detroit, MI 48255, USA
[1] Tel.: 2563728109, fax: 2563725622
E-mail: ashok.batra@aamu.edu

Received: 1 November 2021 /Accepted: 28 November 2021 /Published: 30 November 2021

Abstract: Tremor is a small, rhythmic shaking movement that occurs in a back-and-forth pattern. Everyone has a small, sometimes undetectable, shake when they move their hands. Fatigue, stress, feelings of anger or fear, caffeine, and smoking can make this normal shaking more obvious. Hand tremor can occur at any age but most commonly occurs in middle-aged and older men and women. In the present investigation, a light-weight ring using polyvinylidene fluoride (PVDF) thick films as piezoelectric transducer, were fabricated and tested for monitoring Hand Tremors under voluntary human tremor modes.

Keywords: PVDF, Piezo-ring, Hand tremor.

1. Introduction

Tremor is defined as an involuntary, rhythmic to greater extent, oscillatory movement of a body part. Hand tremor is an involuntary muscle movement, trembling, or shaking of the hands. Short-term tremors that disappear quickly can be due to an anxiety attack or stress; whereas chronic tremors that come and go over a longer period of time can be due to the essential tremor (ET). Essential tremor is a neurological condition that causes your hand to shake rhythmically. However, any type of hand tremor, even if it is temporary, needs to be evaluated, as it can be due to serious, ongoing diseases, such as Parkinson's disease and multiple sclerosis. In particular, a hand tremor on one side of the body can be indicative of brain damage from a tumor or stroke. The amplitude of tremor is often small, such that it can only be measured with a highly responsive and sensitive sensors. Tremor can be further be divided into two very basic groups: physiological and pathological. Physiological tremor is ubiquitous, asymptomatic (normal) shaking that affects everyone and results from activity in individual motor units. It is generally a low amplitude (<0.5 mm peak-to-peak), high frequency movement (between 8 and 12 Hz) that is barely visible such as writing or holding a cup. In certain cases, such as fear or excitement, the tremor might increase in amplitude to such a degree that it interferes with simple actions such as writing or holding something steady, such as holding a coffee cup, writing, etc.

2. Materials and Methods

Pathological tremors, on the other hand, arise because of a disease or disorder, usually of central or peripheral nervous system. These tremors always

involve rhythmical contractions of muscle groups which manifest in a periodic, that is, roughly sinusoidal, movement about an axis. The rhythmic nature of tremor suggests characterization by amplitude, waveform, or frequency. There are several types of abnormal tremor, viz., Resting or Static tremor (frequency: 3 to 6 Hz) occurs in up to 75% of individual with Parkinson disease (PD) patients; Action tremor (3 to 6 Hz) occurs in more than 25% of PD patients; Postural tremor (4 to 12 HZ) occurs in around 60% of PD patients; Task-specific tremor (3 to 10Hz); and isometric tremor (medium frequency). An objective evaluation of tremor severity is needed to record the course of disease and the usefulness of treatment for on-time interventions in clinical trials. Various transducer-based methodologies, such as accelerometry, electro-myography, gyroscopy, electromagnetic tracking, actigraphy, and digitizing tablets are being currently used [1-6]. Due to their size, weight, potential high costs, time consuming measurements and their complexity, most devices are only used in electro-physiological laboratories and are not yet applicable for daily clinical or home monitoring. To mitigate above cited present cumbersome characteristics, we propose a concept of low-cost, light-weight ring with cantilevered piezoelectric sensors as depicted in Fig. 1.

We investigated our prototype piezo-ring's functionality by (a) voluntary rhythmic tremor and (b) random tremor as seen in Fig. 2 (a) and Fig. 2 (b) respectively. From the waveform, one can extract amplitude, frequency, and waveform. Furthermore, Frequency spectra can be used to extract amplitude and signal energy as a parameter for tremor severity.

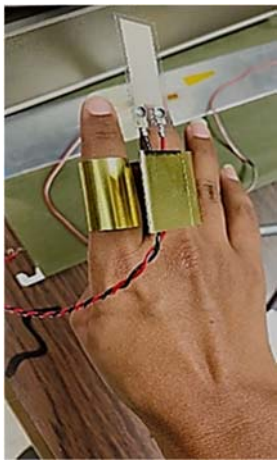

Fig. 1. Light weight metal ring with PVDF type piezo transducer.

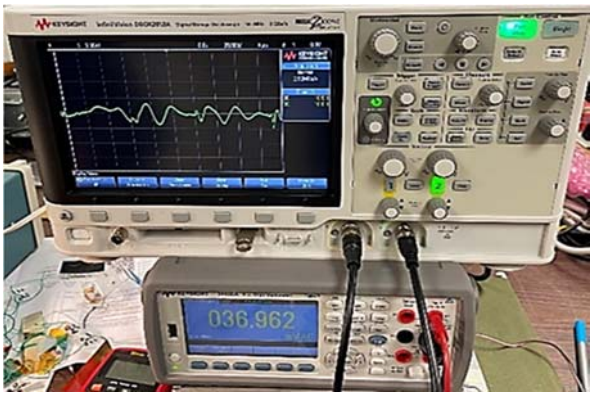

(a)

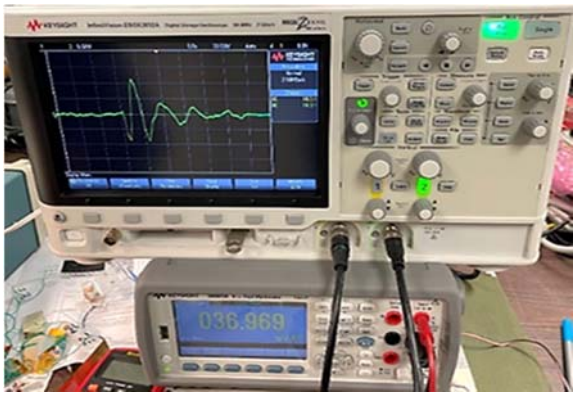

(b)

Fig. 2. Waveform obtained for rhythmic tremor (a), for random tremor (b).

3. Technical Summary of the Proof-of-concept

PVDF can be used as power harvester as well producing power and that can be utilized to power the small associated electronics [7]. Furthermore, results obtained can be correlated with clinical scales. This is a technical, and clinical proof-of-concept device under test (DUT) for its demonstration. Further clinical investigations along with algorithmic wave analysis will demonstrate if tremors can be recorded and analyzed in home-environment and additionally, if it is possible to achieve a home-monitoring system, like blood-pressure measurements.

Acknowledgements

Authors thank Mr. E. Curtis for fabricating the Ring. Special Thanks to Dr. Chance M. Glenn for his comments.

References

[1]. J. S. Lora-Millan, G. Delgado-Oleas, Jullian Benito-Leon and E. Rocon, A review on wearable technologies for tremor suppression, *Frontier in Neurology*, 12, August 2021, pp. 1-17.

[2]. T Zajki-Zechmeister, M. Kogi, K. Kalsberger and et al., Quantification of tremor severity with mobile pen, Heliyon, 6, 8, 2020, e04702.

[3]. A. Channa, R-Cristian Ifrim, D. Popesu and N. Popescu, A-Wear Bracelet for detection of hand tremor and Bradykinesia in Parkinson's patients, *Sensors*, 21, 3, 2021, 981.

[4]. B. Vescio, A. Quattrone, R. Nistico and et al. Wearable devices for assessment of tremor, *Frontier in Neurology*, 12, 202, 1680011.

[5]. H. Abbas, K. Zahed, L. Alic and et al, A wearable, low-cost hand tremor sensor for detecting hypoglycemic events in diabetic patients, in *Proceedings of the 2018 IEEE International RF and Microwave Conference (RFM)*, 2019, pp. 268-271.

[6]. R. J. Elible and J. McNames, Using a portable transducer to measure tremor severity, Tremor and other Hyperkinetic movements, 6, 2016, p. 375.

[7]. S. Palwai, A. Batra, S. Kotru and A. Vaseashta, Electrospun Polyvinylidene Fluoride Nanofiber Membranes Based Flexible Capacitive Sensors For Tactile and Biomedical Applications. *Surface Engineering and Applied Electrochemistry*, Vol. 58, 1, 2022 (In press).

5th International Conference on Optics, Photonics and Lasers (OPAL' 2022)

18-20 May 2022

Tenerife (Canary Islands), Spain

http://www.opal-conference.com

About the Event

Similar to the previous OPAL conferences, the 5th International Conference on Optics, Photonics and Lasers (OPAL' 2022) will incorporate three symposiums covering a broaden range in optics, photonics and lasers, and provide an excellent opportunity to exchange ideas and present latest advancements in these areas. The OPAL 2022 will be organized by the IFSA - a professional, non-profit association serving for industry and academy for 20 years.

The purpose of OPAL' 2022 is bring together leading international researchers, engineers and practitioners interested on any of the optical related technologies. The conference will offer plenary and invited talks, contributed oral and poster presentations, special sessions, tutorials, and exhibitions of commercial products. Social and cultural events will also take place to foster networking among the participants in a friendly manner.

Optics:

- Optical and Fibre Optical Sensors and Instrumentation
- Micro-Opto-Electro-Mechanical Systems (MOEMS)
- Physical Optics
- Optoelectronic Devices, Photonics, Nanophotonics and Biophotonics
- Organic Optoelectronics and Integrated Photonics
- Optical Communications, Switching and Networks
- High-speed Opto-electronic Networking
- Optical Fiber Technology: Materials, Devices and Systems
- Optical Information Processing
- Holography
- Optical Metrology
- Optical Imaging Systems and Machine Vision
- Optical Computing
- Guided Wave Optics
- Optics in Condensed and Soft Matter
- Quantum Optics
- Lasers and Laser Applications
- Nonlinear Optics
- Nano and Micro Optics
- Matter Waves
- Quantum Information
- Bio and Medical Optics
- Optical Materials, Characterization Methods and Techniques
- Optical Methods for Process Control
- Microscopy and Adaptive Optics
- Lasers in Medicine and Biology
- Engineering Applications of Spectroscopy
- Optical Microscopy of Composites

Photonics:

- Photonic Sensors
- Photodetectors
- Photonic Integrated Circuit (PIC)
- Photonic Integration and Packaging
- Photonic Crystals
- Biophotonics
- Microwave Photonics
- Nanophotonics
- Photonic Materials and Metameterials
- Quantum Photonics
- Terahertz Photonics
- Photonic Computing
- Applications of Photonic Technologies

Lasers:

- Laser Science
- Laser and laser optics
- Semiconductor Lasers
- Laser Metrology
- Chemical Gas Lasers
- Fiber Lasers
- Nonlinear Lasers
- Laser Propulsion
- Lasers and LEDs
- Laser Nanotechnology
- Laser Spectroscopy and Microscopy
- Laser Applications
- Lasers in Medicine and Biology

5th International Conference on Optics, Photonics and Lasers (OPAL' 2022)

2022 OPAL

Deadlines:

Submission (2-page abstract):	5 March 2022
Notification of acceptance:	20 March 2022
Registration:	5 April 2022
Camera ready (4-6 pages paper):	15 April 2022

One event - three publications !

1) All registered abstracts will be published in the conference proceedings (USB flash drive edition of published Proceedings with the ISBN), distributed during the conference and submitted for indexing to the Web of Science. The previous OPAL' 2018 - 2021 Conference proceedings were indexed by the Conference Proceedings Citation Index.

2) Authors will be invited to submit full-page extended papers to the special issue of Sensors & Transducers open access journal (ISSN 2306-8515, e-ISSN 1726-5479) for free of charge.

3) The limited number of full-page papers published in the journal will be selected by the Editorial Board to extend for book chapters for the open access Book Series on 'Advances in Optics: Reviews', Vol. 6.

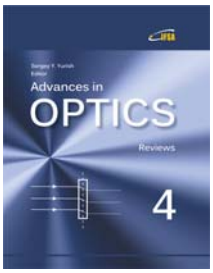

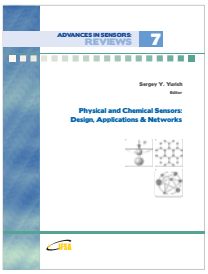

Social Programme

Welcome Cocktail: The Welcome Cocktail will take place on the 16th floor (Sky Lounge Bar) situate on the Hard Rock Hotel's Nirvana Tower building's roof with the best, magnificent, panoramic views to Teide volcano, the Atlantic coast, La Gomera Island and sunset. Actually, it is known as the highest leisure location in Tenerife. Do not miss this opportunity to say the first "hello" to attendees and committee members.

Gala Dinner: The Gala Dinner (BBQ) will take place in the Hard Rock Hotel at the sea beach in front of the Lagoon area.

Contribution Types:

- Keynote presentations
- Invited talks
- Special sessions
- Regular sessions
- Poster session
- Industrial presentations
- Exhibition
- Round tables

Special Sessions:

Participants are welcome to organize and manage special sessions during the conference. Each session will contain 4-6 papers in a related field as specified above.

Session organizers will get:

- Certificate of Appreciation
- Free Registration for the Event
- Special Publishing Theme within Conference Proceedings
- Free article and book chapter post conference publications in appropriate open access journals and 'Advances in Optics: Reviews', Book Series, Vol. 6

Organising Committee

Chairman:

Prof., Dr. Sergey Y. Yurish (IFSA, Spain)

Advisory Chairmen:

Dr. Qiang Wu
(Northumbria University, Newcastle Upon Tyne, UK)
Prof., Dr. Claude Phipps (Photonic Associates, USA)
Prof., Dr. George Semouchkin
(Michigan Technological University, USA)
Prof., Dr. Sandeep Singh Sengar
(University of Copenhagen, Denmark)
Prof., Dr. Boris Mizaikoff (Ulm University, Germany)
Prof., Dr. Mahmoud Daoudi
(National Center for Nuclear Sciences and Technologies, Tunisia)

Conference Manager:

Mrs. Tetyana Zakharchenko
(IFSA Publishing, S.L., Spain)

IFSA Publishing IOP Institute of Physics physicsworld

Call for Chapters

IFSA Publishing

Your Chapter may be in the next Volume of the popular Book Series

ADVANCES IN SENSORS: REVIEWS 8

Open Access Book Series

Sinse 2012

- Physical, chemical and biosensors
- Sensor uncertainty, accuracy, calibration
- Smart sensors and systems
- Intelligent sensors and systems
- Artificial Intelligence enabled sensors
- Virtual and soft sensors
- Sensor instrumentation
- Sensor buses and networks
- Signal processing, sensor fusion
- Nanosensors
- Photonic sensors
- Sensor interfacing and signal conditioning
- Materials for sensors
- MEMS, BioMEMS and NEMS
- Remote Sensors and Telemetry
- Sensor packages and reliability

https://www.sensorsportal.com/HTML/IFSA_Publishing.htm

IFSA

International Frequency Sensor Association Publishing

www.sensorsportal.com

ISSN 1726- 5479